NASA/TM-2017-219596

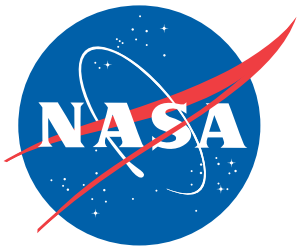

Wind Tunnel Investigation of Passive Porosity Applied to the Leading-Edge Extension and Leading-Edge Flaps on a Slender Wing at Subsonic Speed

Gary E. Erickson
Langley Research Center, Hampton, Virginia

March 2017

NASA STI Program . . . in Profile

Since its founding, NASA has been dedicated to the advancement of aeronautics and space science. The NASA scientific and technical information (STI) program plays a key part in helping NASA maintain this important role.

The NASA STI program operates under the auspices of the Agency Chief Information Officer. It collects, organizes, provides for archiving, and disseminates NASA's STI. The NASA STI program provides access to the NTRS Registered and its public interface, the NASA Technical Reports Server, thus providing one of the largest collections of aeronautical and space science STI in the world. Results are published in both non-NASA channels and by NASA in the NASA STI Report Series, which includes the following report types:

- TECHNICAL PUBLICATION. Reports of completed research or a major significant phase of research that present the results of NASA Programs and include extensive data or theoretical analysis. Includes compilations of significant scientific and technical data and information deemed to be of continuing reference value. NASA counter-part of peer-reviewed formal professional papers but has less stringent limitations on manuscript length and extent of graphic presentations.

- TECHNICAL MEMORANDUM. Scientific and technical findings that are preliminary or of specialized interest, e.g., quick release reports, working papers, and bibliographies that contain minimal annotation. Does not contain extensive analysis.

- CONTRACTOR REPORT. Scientific and technical findings by NASA-sponsored contractors and grantees.

- CONFERENCE PUBLICATION. Collected papers from scientific and technical conferences, symposia, seminars, or other meetings sponsored or co-sponsored by NASA.

- SPECIAL PUBLICATION. Scientific, technical, or historical information from NASA programs, projects, and missions, often concerned with subjects having substantial public interest.

- TECHNICAL TRANSLATION. English-language translations of foreign scientific and technical material pertinent to NASA's mission.

Specialized services also include organizing and publishing research results, distributing specialized research announcements and feeds, providing information desk and personal search support, and enabling data exchange services.

For more information about the NASA STI program, see the following:

- Access the NASA STI program home page at *http://www.sti.nasa.gov*

- E-mail your question to help@sti.nasa.gov

- Phone the NASA STI Information Desk at 757-864-9658

- Write to:
  NASA STI Information Desk
  Mail Stop 148
  NASA Langley Research Center
  Hampton, VA 23681-2199

NASA/TM-2017-219596

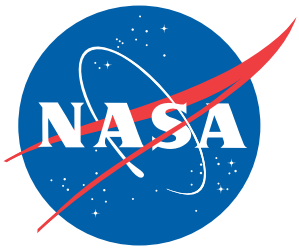

Wind Tunnel Investigation of Passive Porosity Applied to the Leading-Edge Extension and Leading-Edge Flaps on a Slender Wing at Subsonic Speed

Gary E. Erickson
Langley Research Center, Hampton, Virginia

National Aeronautics and
Space Administration

Langley Research Center
Hampton, Virginia 23681-2199

March 2017

Available from:

NASA STI Program / Mail Stop 148
NASA Langley Research Center
Hampton, VA 23681-2199
Fax: 757-864-6500

Table of Contents

Abstract

A wind tunnel experiment was conducted in the NASA Langley Research Center 7- by 10-Foot High Speed Tunnel to determine the effects of passive surface porosity on the subsonic vortex flow interactions about a general research fighter configuration. Flow-through porosity was applied to the leading-edge extension, or LEX, and leading-edge flaps mounted to a 65° cropped delta wing model as a potential vortex flow control technique at high angles of attack. All combinations of porous and nonporous LEX and flaps were investigated. Wing upper surface static pressure distributions and six-component forces and moments were obtained at a free-stream Mach number of 0.20 corresponding to a Reynolds number of 1.35(10^6) per foot, angles of attack up to 45°, angles of sideslip of 0° and +/-5°, and leading-edge flap deflections of 0° and 30°.

Introduction

The control of vortex flows is an important design consideration for military and commercial aircraft, missiles, and launch vehicles. Wings, bodies, stabilizing and control surfaces, engine inlets, and surface protuberances are several sources where controlled flow separation in the form of vortices can occur. Disorganized and/or unsteady flow separation issues are often addressed by adding devices ranging from small vortex generators to energize the local boundary layer to larger wing leading-edge extensions, strakes, and canards to control the global flow field. The aerodynamic benefits of vortex flows can be extended, and undesired effects mitigated, by tailoring the vehicle geometry or incorporating passive and active flow control concepts. The vortex flow topology can be significantly affected by deflected leading-edge devices (reference 1). Passive porosity has been successfully applied to control vortices shed from slender bodies at subsonic through supersonic speeds (reference 2) and to mitigate the adverse effects of shock waves on wings at transonic and supersonic speeds (reference 3). The present experiment focuses on flow-through porosity applied to the leading-edge extension (LEX) and leading-edge flaps of a 65° cropped delta wing to manipulate the leading-edge vortex development and interactions at subsonic speeds. All combinations of porous and nonporous LEX, porous and nonporous leading-edge flaps, and undeflected and deflected flaps were investigated. Figure 1 shows photographs of the model with porous LEX and porous leading-edge flaps installed in the test section of the NASA Langley Research Center (NASA LaRC) 7- by 10-Foot High Speed Tunnel (7- by 10-Foot HST). This model was selected since it was representative of fighter aircraft designs with subsonic and transonic maneuver and supersonic cruise capabilities. Porosity was applied to the LEX, since it was situated ahead of the moment reference center (MRC) and generated a strong vortex flow that affected the global wing flow field. Porosity applied to the leading-edge flaps was expected to significantly affect the interactions of the LEX and wing vortices at high angles of attack. All data contained in this report were obtained with a centerline vertical tail. The primary focus of this report is the interpretation of the wing upper surface static pressure distributions, the longitudinal force and moment aerodynamic coefficients, and the static lateral-directional stability derivatives as a function of the various combinations of LEX and leading-edge flap porosity. The wind tunnel testing was performed in the NASA LaRC 7- by 10-Foot HST in Test 220 at a free-stream Mach number of 0.20, corresponding Reynolds number of 1.35 (10^6) per foot, angles of attack from -2.5° to 45°, and angles of sideslip of 0° and +/-5°.

Nomenclature

ARPBA1.1	chamber area used to compute axial force correction due to average chamber pressure

measurement, 4.9090 square inches (sq. in.)

b span distance, inches (in.)

b_w reference span, 18.726 in. (also *BSPAN1*)

BL model butt line, in.

BMC balance moment center, M.S. 21.465

c local chord length, in.

$c_{r,w}$ wing centerline chord, 23.622 in. (also *CHORD1*)

$c_{t,w}$ wing tip chord, 3.544 in.

$\overline{c}_w$ wing mean aerodynamic chord, 16.056 in.

C_D drag force coefficient, $\frac{Drag}{q_\infty (S_w)}$

C_l rolling moment coefficient, $\frac{Rolling\ Moment}{q_\infty (S_w) b_w}$

C_L lift coefficient, $\frac{Lift\ Force}{q_\infty (S_w)}$

C_m pitching moment coefficient, $\frac{Pitching\ Moment}{q_\infty (S_w) c_{r,w}}$

C_n yawing moment coefficient, $\frac{Yawing\ Moment}{q_\infty (S_w) b_w}$

C_Y side force coefficient, $\frac{Side\ Force}{q_\infty (S_w)}$

C_p static pressure coefficient, $(p - p_\infty)/q_\infty$

$C_{p,u}$ upper surface static pressure coefficient

C_{l_β} lateral stability derivative, $\frac{C_{l\,(\beta = \text{ max positive})} - C_{l\,(\beta = \text{ max negative})}}{\beta_{\text{max positive}} - \beta_{\text{max negative}}}$

C_{n_β} directional stability derivative, $\frac{C_{n\,(\beta = \text{ max positive})} - C_{n\,(\beta = \text{ max negative})}}{\beta_{\text{max positive}} - \beta_{\text{max negative}}}$

C_{Y_β} side force stability derivative, $\frac{C_{Y\,(\beta = \text{ max positive})} - C_{Y\,(\beta = \text{ max negative})}}{\beta_{\text{max positive}} - \beta_{\text{max negative}}}$

DESL data engineering scripting language

ESP electronically-scanned pressure

$l_{0.25\overline{c}}$ tail length, distance between 25% tail mean aerodynamic chord to MRC, in.

LEX leading-edge extension

Mach free-stream Mach number

MRC moment reference center, M.S. 21.144

MS. model station, in.

p local static pressure, pounds per square foot (psf)

p_∞ free-stream static pressure, psf

psf pounds per square foot

psid pounds per square inch differential

PCU pressure calibration unit

q_∞ free stream dynamic pressure, psf

QFlex gravity sensing servo accelerometer

Re Reynolds number, millions per foot

s local semispan measured from the wing centerline, in.

S area, square inches (sq. in.)

S_w reference wing area, 254.3553 sq. in. (also *SAREA1*)

V vertical tail volume, cubic inches (cu. in.)

WL model water line, in.

x local axial distance measured along the wing centerline chord from the wing apex, in.

XBAR1 moment transfer distance

	measured in the body axis system from the BMC to MRC, positive in direction of positive thrust, 0.667 in.
y	local semispan distance measured from the wing centerline, positive to the right, in.
YBAR1	moment transfer distance measured in the body axis system from the BMC to MRC, positive in direction of positive side force, 0.0 in.
ZBAR1	moment transfer distance measured in the body axis system from the BMC to MRC, positive in direction of positive normal force, 0.984 in.
α	angle of attack, degrees
β	angle of sideslip, degrees
λ	taper ratio
Λ_{LE}	leading-edge sweep angle, deg
Λ_{TE}	trailing-edge sweep angle, deg

Subscripts

cl	centerline
flap	leading-edge flap
lex	leading-edge extension
r	root
t	tip
w	wing

Model Description and Test Apparatus

A generic fighter model featuring a 65° cropped delta wing with sharp leading edges was used in this test. The model was designed and fabricated in the 1980s for surface pressure and force and moment testing in subsonic, transonic, and supersonic wind tunnel facilities in support of a multinational Euler code validation program (reference 4) that focused on the prediction of vortex flow effects on slender wings at high angles of attack. The primary configurations that were tested in this program included the isolated wing with different leading-edge geometries (for example, round versus sharp) and a canard-wing arrangement. The model was subsequently used in a cooperative vortex flow aerodynamics research program in the 1980s and 1990s involving NASA Ames Research Center (NASA ARC), NASA LaRC, and the United States Air Force (USAF) Wright Aeronautical Laboratories. As part of this cooperative program, the model was tested in the NASA ARC 6- by 6-Foot Transonic/Supersonic Wind Tunnel (reference 5), NASA LaRC 7- by 10-Foot HST (reference 6), NASA LaRC Unitary Plan Wind Tunnel (UPWT) (reference 7), and NASA LaRC 8-Foot TPT (reference 8). Photographs of the model installed in the NASA LaRC 7- by 10-Foot HST for Test 220 discussed in this report were previously shown in figure 1. The wing had an NACA 64A005 airfoil section from the 40 percent chord station to the trailing edge. A sharp leading edge was obtained by fairing a biconvex circular-arc section into the NACA profile from the 40 percent chord station to the wing leading edge. The wing was mounted in a high position on a fuselage that served as an enclosure for surface pressure and strain gauge balance instrumentation. In the isolated wing configuration, the fuselage tapered down to a small radius along approximately the forward 35-percent portion of its length, and it terminated 0.50 inches (model scale) from the apex of the wing. This portion of the fuselage could be replaced with an alternate forward fuselage section having an integral strut, or “gooseneck.” The model as designed in the 1980s included the installation of a 60-degree swept canard to the gooseneck to provide a closely-coupled coplanar canard-wing arrangement. Initial modifications that were made to the model as part of the NASA and USAF cooperative research program included a wing LEX mounted to the gooseneck in a coplanar arrangement with the wing, a centerline vertical tail on the fuselage, and twin vertical tails mounted to the wings. The LEX was a flat-plate with 0.25-inch thickness, a 65-degree/90-degree planform, and symmetrically-beveled leading edges. The exposed area of the LEX (left and right sides) was 15 percent of the

reference wing area. The LEX incorporated a pattern of 0.050-inch diameter through holes spaced 0.10 inch apart on center to provide a total porosity level of 14.75 percent relative to the LEX exposed area. The fuselage and wings were modified with pockets to allow the installation of a centerline vertical tail or twin vertical tails with integral mounting pads. A later modification to the model featured flat-plate bolt-on leading-edge flaps with 0.25-inch thickness, a 30-degree/65-degree/90-degree planform, and symmetrically-beveled leading edges. Separate mounting brackets allowed the flaps to be mounted to the wing in an undeflected position and with a 30-degree deflection measured normal to the wing leading edge. The total exposed area of the left and right flaps was approximately 12 percent of the reference wing area. The flaps incorporated the same pattern of 0.050-inch diameter through holes spaced 0.10 inch apart on center to provide a total porosity level of 13.5 percent relative to the flap exposed area. Planview and sideview sketches of the wing, LEX, flaps, fuselage, and centerline trail are provided in figure 2 and figure 3, respectively. Note that the bevels along the LEX and flap leading and side edges were not porous because of constraints in the machining process that precluded drilling holes near the edges. In addition, a 0.625-inch wide strip along the centerline of the LEX was solid, since the LEX was bolted to the gooseneck in this region. Similarly, a 0.75-inch wide strip along each trailing edge of the LEX was solid where the LEX overlapped the wing leading edge in a tongue-and-groove arrangement. There were two 0.20-inch wide sections on each flap that were solid where the mounting brackets attached to the flaps. Furthermore, the flaps were solid along a 0.125-inch wide strip where the flaps overlapped the wing leading edge in a tongue-and-groove arrangement. The LEX and flaps were tested with 0 percent porosity (solid LEX and solid flaps) by applying sealing tape having 1.8 mil thickness (0.0018 inches) along the lower surface to cover all of the through holes. Geometric details of the model are summarized in Table I.

The right wing upper surface was instrumented with a total of sixty four (64) 0.020-inch diameter pressure orifices distributed in three spanwise rows. Of the 64 available orifices, 47 were selected to populate a single 48-port ESP module. The pressure rows were located at 30 percent, 60 percent, and 80 percent of the distance, x, along the wing centerline chord, $c_{r,w}$, measured from the apex of the wing ($x/c_{r,w}$ = 0.30, 0.60, and 0.80, respectively). A sketch of the pressure orifice layout is shown in figure 2, and the pressure orifice locations are listed in Table II. The bolt-on flaps were not instrumented with pressure orifices. The pressure orifice locations are referenced to the wing local semispan at $x/c_{r,w}$ = 0.30, 0.60, and 0.80 with the leading-edge flap removed to be consistent with previous testing of this model (references 5, 7, and 8). The orifice nondimensional semispan location, y/s, is expressed in terms of the semispan distance, y, measured from the wing centerline divided by the wing local semispan, s. Consequently, y/s values of 0.0 and 1.0 correspond to the wing centerline and the right wing leading edge without flap, respectively. The presence of the leading-edge flap extended the local semispan by approximately 1.17 inches at $x/c_{r,w}$ = 0.30 and 0.60 and by 0.55 inches at $x/c_{r,w}$ = 0.80. This corresponded to respective increases in the local semispan at the three chordwise stations of approximately 35.4%, 17.7%, and 6.2%, respectively. Test 220 in the 7- by 10-Foot HST featured 18 orifices at $x/c_{r,w}$ = 0.30, 15 orifices at $x/c_{r,w}$ = 0.60, and 14 orifices at $x/c_{r,w}$ = 0.80. The distribution of taps in each row was intended to capture the pressure signature of a leading-edge vortex at high angles of attack. The pressures were measured using a single 48-port, 15 psid electronically-scanned pressure (ESP) module located inside the model as shown in figure 3. The 0.040-inch outer diameter (O.D.) stainless steel pressure lines inside the model were connected to the ESP module using 0.040-inch O.D. urethane jumpers. One thermocouple wire was attached to the side of the ESP module to monitor the module surface temperature. The ESP electronics cable, reference and calibration pressure lines, and

thermocouple wire were routed through channels machined into the internal balance strongback and then out along the model sting. The instrumentation bundle was then encased in protective plastic spiral wrap and fiberglass tape that extended along the model support system to an ESP interface box that was positioned outside the test section.

The model forces and moments were measured in Test 220 using a NASA LaRC internally-mounted, six-component strain gauge balance designated 842A. A full balance calibration was performed prior to the entry in the 7- by 10-Foot HST (calibration date: October 23, 1991). The balance design loads and calibration accuracies are presented in Table III. The calibration accuracies expressed as aerodynamic coefficients based on the test conditions in Test 220 are presented in Table IV. A sketch of the balance inside the model was previously shown in figure 3. The balance wiring was routed internally to the sting. The balance moment center (BMC) was located at model station (MS) 21.465, which corresponded to approximately 58.1 percent of the distance along the wing centerline chord measured from the wing apex ($x/c_{r,w}$ = 0.581). The MRC was taken about the 57 percent centerline chord location ($x/c_{r,w}$ = 0.57) or MS 21.144 as shown in figure 3. The force and moment coefficients for all configurations were based on the reference wing area, S_w, that does not include the added area of the bolt-on leading-edge flaps.

The model base area was negligible, and base pressures were not measured in Test 220. Two 0.040-inch O.D. stainless steel tubes were run externally and diagonally opposed along the sting and extended inside the model fuselage cavity. One chamber pressure tube terminated approximately 0.5 inches aft of the balance-to-sting draw nut, and the second chamber pressure tube terminated 2.0 inches forward of the fouling strip. The tubes were connected to individual 2.5 psid pressure tranducers located in the plenum region surrounding the test section. The pressure transducers were calibrated during the model installation process.

The NASA LaRC sting number 18 served a dual role of providing an internal passageway for the balance wiring bundle and adapting the model and balance assembly to the tunnel support hardware. The sting was a taper fit to the 7- by 10-Foot HST motorized roll coupler, which was installed in a high angle-of-attack static stability main support system. The roll coupler and the pitch mechanism in the main support system were calibrated during the model installation process.

Transition grit was not applied to the model, since the flow was assumed to separate at the sharp leading edges at all conditions of interest in the current experiment. In addition, a suitable gritting strategy based on the criteria in reference 9 to cause transition of the boundary layer associated with vortex-induced reattached flow on the wing upper surface has not been established. Reference 10 summarizes many of the challenges associated with transition grit applications for high angle-of-attack experimentation.

A fouling strip circuit was installed on the sting near the model base. Model-to-sting fouling was not encountered at any of the wind-on conditions in Test 220.

Wind Tunnel Facilities and Test Conditions

The investigation was conducted in the NASA LaRC 7- by 10-Foot HST and was designated Test 220. Photographs of the general research fighter model installed in the 7- by 10-Foot HST test section were previously shown in figure 1. The NASA LaRC 7- by 10-Foot HST was a continuous-flow, subsonic-transonic atmospheric facility. In the closed test section configuration, the speed range was from approximately Mach = 0.06 to Mach = 0.94 depending on the model size. The test section was approximately 6.584 feet high by 9.574 ft wide, and the mean cross-sectional area of the test section for use in blockage calculations was 62.1256 square feet.

The tunnel operated at ambient temperature and pressure and continuously exchanged air with the surrounding atmosphere. The test conditions at Mach = 0.20 in the NASA LaRC 7- by 10-Foot HST corresponded to a nominal Reynolds number of approximately $1.35(10^6)$ per foot and a free-stream dynamic pressure of 58 pounds per square foot (psf). Reference 11 provides a detailed description of the calibration, operation, and testing capabilities of the NASA LaRC 7- by 10-Foot HST. This facility was permanently closed in 1994.

The model angle of attack and angle of sideslip were determined via appropriate Euler angle transformations using the output from an accelerometer mounted at the base of the 7- by 10-Foot HST high angle-of-attack support system, the output from a potentiometer installed in the motorized roll coupler, balance-to-support system and balance-to-model misalignment angles, and corrections applied to account for aeroelastic or mechanical deflections of the model, balance, and support system assembly due to aerodynamic loads. The desired tolerances for the angle of attack and sideslip setpoints were typically +/-0.25 degrees and +/-0.5 degrees, respectively.

ESP and six-component force and moment measurements were simultaneously obtained at Mach = 0.20 for all configurations presented in this report. Previous testing experience with this model in references 5, 7, and 8 indicated that sufficient slack could be provided in the ESP wiring and tubing bundle extending from the routing channels in the balance strongback to the sting to mitigate the effects of bridging the balance on the force and moment measurements. The nominal angle of attack range was -2.5° to +45° in 2.5° increments. Angle-of-attack sweeps were conducted at sideslip angles of 0° and +/-5°. The angle-of-attack sweeps were performed in a pitch-pause mode. The Experimental Techniques section describes the ESP and force and moment measurement techniques in more detail.

Experimental Techniques

ESP Measurements

Surface static pressure measurements were obtained at 47 discrete locations on the model using a single, internally-mounted 48-port ESP module. The remaining port was dedicated to a reference pressure line. The 7- by 10-Foot HST ESP system featured System 780B data acquisition instrumentation manufactured by Pressure Systems, Incorporated. The System 780B was interfaced with the wind tunnel data acquisition system and used external modules or modules mounted internally to the model. The internal volume of the 65-degree cropped delta wing model was sufficient to contain a single 48-port, 15 psid ESP module. A 15 psi pressure calibration unit (PCU) was used in this experiment with a digitally-controlled pneumatic source that provided valve control and generated calibration pressures for the ESP scanner. The ESP module pressure measurement accuracy was assumed to be +/-0.05% full-scale (FS). The ESP module pressure range was selected on the basis of prior subsonic testing of this model with solid LEX (reference 5). The uncertainties for this module expressed in terms of the static pressure coefficient for the test conditions that were run in 7- by 10-Foot HST Test 220 are listed in Table V. Insufficient data were acquired in Test 220 to conduct a within-test data repeatability assessment. However, a detailed assessment of tunnel-to-tunnel data reproducibility was performed in reference 8, where the wing upper surface static pressure distributions obtained at Mach = 0.50 on the 65-degree cropped delta wing model in previous testing in the 7- by 10-Foot HST and the NASA LaRC 8-Foot Transonic Pressure Tunnel (TPT) were compared. Reproducibility of the surface static pressure coefficients at angles of attack up to 30 degrees was typically within 1% to 2% of the FS range of the ESP module, depending on the configuration (wing-alone, wing with solid or porous LEX, centerline tail versus twin wing-mounted tails). Data scatter was typically higher with the porous LEX because of unsteady flow through the 0.050-inch diameter holes in the LEX. The tunnel-to-

tunnel data scatter is not an unexpected result, since the 7- by 10-Foot HST and 8-Foot TPT testing was conducted at high angles of attack where model dynamics occurred and different pressure measurement instrumentation, model support systems, and testing environments existed in each facility.

The ESP data acquisition rate during the testing was 10 frames per second for 2 seconds, for a total of 20 frames per data point. A dwell time of 5 seconds was specified to allow the pressures to stabilize before acquiring a data point.

The standard ESP calibration consisted of five points that were used to determine a quartic polynomial representation of the pressure-voltage signature of each transducer or sensor. Full wind-on calibrations were performed prior to each run series once the ESP module temperature had stabilized.

Strain Gauge Balance Measurements

Force and moment data were obtained in Test 220 with a 6-component electrical strain gauge balance designated NASA LaRC 842A. The 842A balance design loads and the balance calibration accuracies (95% confidence level) expressed in percent full-scale (% F. S.) were previously shown in Table III. The balance accuracies were converted to microvolts (μV) and, also, to pounds (lbs) or inch-pounds (in-lbs) as shown in Table IV. The latter values were used to estimate the measurement accuracies expressed as aerodynamic force and moment coefficients for the conditions in Test 220 as shown in Table IV. The tunnel-to-tunnel reproducibility of the aerodynamic force and moment coefficients at Mach = 0.50 in reference 8 was generally within 0.5% and 1.0%, respectively, of the FS range of the balance, depending on the model configuration.

The balance data acquisition rate during the testing was 30 frames per second for 2 seconds, for a total of 60 frames per data point. All force and moment data were acquired in a pitch-pause mode. A dwell time of 5 seconds at each setpoint was dictated by the simultaneous acquisition of the ESP data.

Force and moment and surface pressure measurements were simultaneously obtained despite the bridging of the balance with the on-board ESP cable, reference and calibration pressure lines, and thermocouple wire. Precautions were taken to mitigate any bridging effects on the balance force and moment measurements by distributing the ESP instrumentation bundle through the routing channels in the balance strongback and providing a flexible bridge from the model to the sting. Calibrated weights were placed at known locations on the model to apply prescribed values of the normal force, pitching moment, and rolling moment. A hand-held force gauge was also used to apply check loads to all six force and moment components. The applied loads were compared to the computed loads from the wind tunnel data system, which indicated that simultaneous acquisition of the balance and ESP measurements was a valid testing approach in the current application.

Model Chamber Pressure Measurements

Model chamber pressures were measured at two diagonally-opposed locations approximately 0.5 inches downstream of the balance-to-sting draw nut. The 0.040-inch outer diameter (O.D.) stainless steel pressure tubes were run along the sting and model support system and routed to the plenum region surrounding the test section where they connected to individual 2.5 psid pressure transducers. The manufacturer-specified measurement accuracy (95% confidence level) as a percent of full-scale is +/-0.1% for these transducers (+/-0.0025 psid).

Pitch Angle Measurements

The primary type of instrumentation in use at the 7- by 10-Foot HST for pitch angle measurement was a gravity-sensing servo accelerometer (QFlex). Direct and indirect methods of model attitude measurement were used. The direct measurement used an accelerometer mounted in

the model. The indirect measurement featured an accelerometer installed at the base of the high angle-of-attack static stability support system with corrections applied to account for aeroelastic or mechanical deflections of the model, balance, sting, and support system component assembly. There was insufficient internal volume in the 65-degree cropped delta wing model to accommodate a QFlex package. Consequently, the indirect method of attitude measurement was used in Test 220. For static (unaccelerated) model conditions, the QFlex measures changes in angle relative to the horizontal by determining the differences in the component of the force due to gravity acting parallel to its sensitive axis. Although the instrument response to acceleration is linear, its response to changes in attitude relative to the local gravity vector in unaccelerated conditions is sinusoidal. The QFlex calibration was performed by installing a digital inclinometer to the precision-machined LEX upper surface. A 14-point calibration was performed at pitch angles from approximately -2.5 degrees to a maximum static pitch angle of +42.5 degrees. The standard deviation from the QFlex calibration was approximately 0.005 degrees. Since models in the 7- by 10-Foot HST were normally forward of the main support system center of rotation, the model nose could approach the tunnel ceiling as the model rotated to high angles of attack. Measurements were taken from the test section ceiling to the apex of the model LEX at the highest pitch angles during the QFlex calibration. At a pitch angle of +42.5 degrees, the LEX apex was approximately 15 inches from the ceiling.

Corrections to account for aeroelastic or mechanical deflections of the model, balance, and sting assembly due to aerodynamic loads were based on in-tunnel sting and balance deflection calibrations. Deflections due to normal force, pitching moment, rolling moment, side force, and yawing moment were obtained using calibrated weights suspended on a pan and attached to the balance calibration fixture via a double knife-edge assembly. Prescribed loads were applied at predetermined locations relative to the BMC, and the corresponding deflections were recorded using a digital inclinometer installed on the balance calibration fixture and referenced to the QFlex in the main support system. The sting deflection calibrations also provided an opportunity to check the data acquisition and data reduction system by comparing the applied loads to the computed loads.

Roll Angle Measurements

The 7- by 10-Foot HST motorized roll coupler provided the primary measurement for the model roll angle. Output from the roll coupler was obtained using an onboard potentiometer. The roll coupling was calibrated using a digital inclinometer mounted to the balance calibration fixture.

Corrections

Flow angularity

Several previous tests of three-dimensional (3-D) models in the 7- by 10-Foot HST indicated that flow angularity in the test section was small and was typically less than approximately 0.05 degrees. Consequently, flow angle runs were not performed in Test 220, and the force and moment data were not corrected for the assumed small effects of tunnel flow angularity.

Jet boundary and blockage

Jet boundary and blockage corrections were applied to the test data from the 7- by 10-Foot HST that are presented in this report according to the procedures in reference 12 and reference 13.

Chamber pressures

The model chamber pressure measurements were used to correct the balance axial force to a condition of free-stream static pressure at the model base. Base pressure corrections were not applied, since the model base area was essentially zero.

Previous Flow Visualization Results

Laser Vapor Screen

The 65-degree cropped delta wing model with solid and porous LEX was previously tested in the NASA LaRC 8-Foot TPT in reference 8. A laser vapor screen technique was used (reference 6) to visualize the condensation patterns in cross planes above the wing corresponding to the locations of the three rows of pressure orifices at $x/c_{r,w}$ = 0.30, 0.60, and 0.80. Flow visualization images at $x/c_{r,w}$ = 0.80 from reference 8 are shown in figure 4 with the solid LEX and porous LEX at Mach = 0.85 and α = 16, 20, 24, and 28 degrees. The solid LEX configuration is characterized by distinct LEX and wing vortex flows having approximately circular cross sections that exhibit a strong mutual, or direct, interaction, including a coiling of the vortices at the higher angles of attack. This direct interaction is more pronounced at lower subsonic Mach numbers (reference 6). LEX porosity shifts the dominance from the LEX vortex to the wing vortex by reducing the vorticity shed from the LEX leading edge (reference 8). The LEX vortex is not apparent in any of the porous LEX images, which feature an apparent single diffused, but stable, wing vortex. Porosity does not suppress the LEX vortex flow; however, it is so weak that condensation does not occur in sufficient quantity to render it visible in the vapor screen images.

The current investigation extends the application of passive porosity to manipulate the development of the wing leading-edge vortex with bolt-on leading-edge flaps, either independent of, or in combination with, passive manipulation of the LEX vortex. The laser vapor screen flow visualization technique was available in the 7- by 10-Foot HST (reference 6). However, its implementation was not practical at Mach = 0.20, because of the prohibitive amount of water injection into the tunnel circuit to yield local condensation within the vortex flows. Consequently, interpretation of the surface pressure and internal strain gauge balance measurements in this report is more speculative, with support from previous testing of similar configurations.

Discussion of Results

Data plots created using data engineering scripting language (DESL) scripts (reference 14) are presented in this section that represent an extensive sampling of the results obtained in the 7- by 10-Foot HST Test 220. Several basic plot formats are used to illustrate the upper surface static pressure coefficient distributions at selected angles of attack and the longitudinal aerodynamic force and moment coefficients and the static lateral-directional stability derivatives in angle-of-attack sweeps. All plots compare the test results obtained on the four possible combinations of solid and porous LEX and leading-edge flaps. Separate sets of plots are presented corresponding to the leading-edge flaps undeflected and deflected to 30 degrees. The wing pressure distributions are plotted in the three spanwise rows superimposed onto an isometric view of the right-hand LEX, wing, and leading-edge flap. The longitudinal aerodynamic coefficients in the stability axis system are plotted as C_L versus angle of attack, α, C_L versus C_D, and C_L versus C_m. The static lateral-directional stability derivatives in the stability axis system (C_{l_β}, C_{n_β}, C_{Y_β}) are plotted versus α. The data plots are presented in three major sections containing, respectively, the wing upper surface static pressure distributions, the longitudinal aerodynamic force and moment coefficients, and the static lateral-directional stability derivatives.

Pressure Distributions

Leading-edge flaps undeflected

Figure 5 shows the wing upper surface static pressure distributions obtained with all combinations of LEX and undeflected leading-edge flap porosity at nominal angles of attack of 10, 15, 20, 25, 30, 32.5, 35, and 40 degrees. The results obtained at α = 10° are the least informative, since the LEX and wing vortex-induced effects are more subtle at this angle of attack. However, their inclusion in figure 5 is

intended to assist in the interpretation of the flow-field development at the higher angles of attack. The data symbols are color-coded to better discern the differences in the pressure distributions at each angle of attack. The configuration with solid LEX and solid leading-edge flaps is a baseline represented by closed, black circle symbols. Open green square symbols correspond to the solid LEX and porous flaps. Open red diamond symbols represent the configuration with porous LEX and solid flaps. Finally, open blue triangle symbols denote the configuration with porous LEX and porous flaps. Planview illustrations of all four configurations are also shown, where the shaded regions on the LEX and flaps denote when porosity is applied.

The dual surface pressure footprints of the LEX vortex and wing leading-edge vortex on the baseline configuration are most apparent in the data at $\alpha = 15°$ and $x/c_{r,w} = 0.60$ and 0.80 (figure 5(b)). These results are qualitatively consistent with the laser vapor screen images from reference 8 at $\alpha = 16°$ and 20° and Mach = 0.85 previously shown in figure 4 for the solid LEX and wing without flaps. The most probable source of the single suction pressure peak at $x/c_{r,w} = 0.30$ is the LEX vortex, since the wing vortex is likely very small and situated outboard of the pressure orifices at this measurement station. The initial development of the wing leading-edge vortex with undeflected flap will differ from the configuration tested in reference 8, because of the planform break along the flap apex and an outboard displacement of the wing vortex relative to the LEX vortex. Vorticity is shed from the leading edge of the flap apex, which will either combine with the vortex development beginning at the 65-degree planform break along the wing leading edge or be entrained into the LEX vortex. A water tunnel flow visualization investigation of a 0.025-scale Northrop-Grumman F-5E model (reference 15), which featured a LEX planform similar to the flap apex on the current configuration, revealed vortex shedding from each leading edge segment, which combined into a single vortex before traversing the main wing flow field. Direct interaction of the LEX and wing vortices is inferred from the baseline configuration pressure distributions at $\alpha = 20°$ (figure 5(c)), where the interwining vortices at $x/c_{r,w} = 0.60$ and 0.80 induce a single suction pressure peak at each measurement station. This trend is also consistent with the coiling of the LEX and wing vortices depicted in the laser vapor screen images from reference 8 at $\alpha = 24°$ and 28° and Mach = 0.85 in figure 4. The persistence of individual vortex cores that orbit about it each represents a reasonable balance between the LEX and wing vortices on the baseline configuration. The pronounced single suction pressure signatures persist up to $\alpha = 32.5°$ (figure 5(f)). At $\alpha = 35°$ (figure 5(g)), the advance of vortex breakdown over the wing promotes a significant decrease in the maximum suction pressure peaks and a broadening of the pressure distributions. This trend continues at $\alpha = 40°$ (figure 5(h)). These results provide a basis to infer the effects of LEX and flap porosity on the vortex-induced surface pressure distributions that are now discussed.

The dual vortex pressure signatures that were observed on the baseline configuration at $\alpha = 15°$ and $x/c_{r,w} = 0.60$ and 0.80 are less apparent when porosity is applied to the undeflected leading-edge flap (figure 5(b)). Porosity reduces the vorticity shed from the leading edge, which weakens the wing vortex. Consequently, the diffused wing vortex will be broader and move inboard (references 7 and 8) to interact and, perhaps, combine with the dominant LEX vortex. This interaction between the two disparate vortex systems yields single vortex suction pressure peaks at $\alpha = 20°$ and $x/c_{r,w} = 0.60$ and 0.80 (figure 5(c)) with diminished suction pressure maxima compared to the baseline configuration. In addition, the location of the suction peaks is displaced inboard as a result of the reduced influence of the wing vortex. There is no significant effect of leading-edge flap porosity on the pressure distributions at $x/c_{r,w} = 0.30$, since this forward pressure row is less exposed to the global influence of flap porosity. These trends persist up to $\alpha = 30°$ (figure 5(e)). At $\alpha = 32.5°$ (figure 5(f)), however, the data suggest an earlier

onset of vortex breakdown over the wing, since the pressure distributions with the porous flap exhibit a marked decrease in the suction pressure peaks and overall suction pressure levels at all three measurements stations compared to the baseline configuration. The LEX and wing vortices on the baseline configuration have a synergistic effect such that both vortices are more stable together than in isolation. The balance between the LEX and wing vortices is altered by flap porosity, which weakens the wing vortex, reduces this synergistic effect, and promotes earlier onset of vortex breakdown. The suction pressure levels partially recover at α = 35° (figure 5(g)), and the differences in the pressure distributions between the baseline and porous flap configurations diminish as vortex breakdown advances over both configurations. A similar trend is observed at α = 40° (figure 5(h)). A possible explanation for the discontinuous trend in the pressure distributions with the porous flap at α = 32.5° through α = 40° is the abrupt onset of asymmetric vortex breakdown at the nominal zero-sideslip condition, which can occur on very slender configurations at high angles of attack (reference 15). Slight differences in the array of through-holes in the left and right leading-edge flaps could trigger asymmetric vortex breakdown. In this case, the vortices may exhibit stability into the near wake of the wing on one side and be unstable (burst) on the other side. Restoration of flow symmetry occurs at a higher angle of attack when the longitudinal adverse pressure gradient along the wing overwhelms any geometric asymmetries. As the previously stable vortex system on one side breaks down over the wing, a slight downstream shift in the position of vortex breakdown may occur on the other side, resulting in a partial recovery of the vortex-induced suction pressure levels.

Adding porosity to only the LEX yields single vortex suction pressure signatures at α = 15° and $x/c_{r,w}$ = 0.60 and 0.80 (figure 5(b)) but, in this case, the suction peaks are dominated by the vortex shed from the solid leading-edge flap. LEX porosity reduces the strength of the LEX vortex to promote a wing vortex-dominated flow field. In addition, the overall suction pressure level is higher at $x/c_{r,w}$ = 0.30 compared to the baseline configuration. It is assumed that the weaker, diffused LEX vortex is also broader and closer to the wing surface (references 7 and 8), so that it induces higher local suction pressures at this measurement station. The single suction peaks induced by the wing vortex-dominated flow field are also apparent in the pressure distributions at α = 20° and $x/c_{r,w}$ = 0.60 and 0.80 (figure 5(c)). These suction peaks are located farther outboard compared to the peaks associated with the porous flap configuration previously discussed. This provides a good example of the modulation of the relative strengths of the LEX and wing vortices due to porosity applied to either component. The diminished influence of the porous LEX vortex on the wing flow field is apparent in the pressure distributions at α = 25° (figure 5(d)), α = 30° (figure 5(e)), and α = 32.5° (figure 5(f)), where the reduced suction peak magnitudes and overall suction pressure levels at $x/c_{r,w}$ = 0.60 and 0.80 suggest early onset of vortex breakdown over the wing. The differences in the pressure distributions at these measurement stations diminish at α = 35° (figure 5(g)) and α = 40° (figure 5(h)) as vortex breakdown also advances over the baseline configuration.

.

Adding porosity to the LEX and leading-edge flaps promotes single vortex suction pressure signatures at α = 15° and $x/c_{r,w}$ = 0.60 and 0.80 (figure 5(b)), which are attributed to weakly-interacting LEX and wing vortices. The suction peak magnitudes and locations at these measurement stations are intermediate to those obtained with the porous LEX-only and porous flap-only configurations. Similar trends are observed at α = 20° (figure 5(c)), except at $x/c_{r,w}$ = 0.80, where the peak suction pressures are lower compared to either of the porous LEX or porous flap configurations. The flatter pressure distribution at α = 25° and $x/c_{r,w}$ = 0.80 and the corresponding decrease in overall suction pressure level at $x/c_{r,w}$ = 0.60 suggest the onset of vortex breakdown over the wing. The forward advance of vortex breakdown appears more rapid

as the angle of attack increases. At α = 35° (figure 5(g)), for example, the pressure distributions at all three measurement stations are influenced by vortex breakdown effects, since the weaker interacting vortex flows are unable to navigate the adverse pressure field over the wing in a stable manner.

Leading-edge flaps deflected 30 degrees

Figure 6 shows the wing upper surface static pressure distributions obtained with all combinations of LEX and deflected leading-edge flap porosity at nominal angles of attack of 10, 15, 20, 25, 30, 32.5, 35, and 40 degrees. The data symbols are color-coded in the same manner as in figure 5 corresponding to the undeflected leading-edge flap. In this section, the baseline configuration corresponds to the solid LEX and solid flap, with the flap deflected to 30 degrees.

The deflected leading-edge flap delays the direct interaction of the LEX vortex and wing vortex on the baseline configuration to higher angles of attack, since the wing vortex is partially constrained in size and inboard movement. For example, dual vortex pressure signatures are apparent in the data at α = 20° and $x/c_{r,w}$ = 0.60 and 0.80 (figure 6(c)). Similar pressure signatures can also be inferred at α = 25° (figure 6(d)), although the data at $x/c_{r,w}$ = 0.80 are more subtle. Direct interaction of the LEX and wing vortices is consistent with the single suction pressure signature at α = 30° (figure 6(e)) and $x/c_{r,w}$ = 0.80. However, two local suction pressure peaks are still evident in the pressure distribution at $x/c_{r,w}$ = 0.60. The upstream influence of vortex breakdown over the wing is suggested by the decrease in overall suction pressure levels at $x/c_{r,w}$ = 0.60 and 0.80 as the angle of attack increases from 32.5° (figure 6(f)) to 35° (figure 6(g)). Vortex breakdown effects are clearly apparent in the pressure distributions at all measurement stations at α = 40° (figure 6(h)).

The deflected leading-edge flap is less effective in containing the wing vortex when porosity is applied to the flap. At α = 15° and $x/c_{r,w}$ = 0.60 and 0.80 (figure 6(b)), for example, the pressure signature of the weakened wing vortex is less pronounced and situated farther inboard compared to the baseline configuration. At α = 20° and $x/c_{r,w}$ = 0.60 (figure 6(c)), the individual footprints of the LEX and wing vortices are subtle, but the single broad suction pressure plateau at $x/c_{r,w}$ = 0.80 suggests the weaker wing vortex is combining with the more dominant LEX vortex. The latter effect is more pronounced at α = 25° (figure 6(d)) and α = 30° (figure 6(e)), where the pronounced single suction pressure signatures at $x/c_{r,w}$ = 0.60 and 0.80 are induced by a combined LEX and wing vortex system. The porous deflected flap configuration exhibits an abrupt onset of vortex breakdown at α = 32.5° (figure 6(f)), where the vortex-induced suction pressures are significantly lower than the baseline configuration. However, a partial recovery occurs in the overall suction pressures at α = 35° (figure 6(g)) to levels that are comparable to those obtained on the baseline configuration. This trend, which is attributed to the transient effects of zero-sideslip flow asymmetries, is similar to that observed with the porous undeflected leading-edge flap in figure 5(f) and figure 5(g). Clear evidence of vortex breakdown on the baseline and porous flap configurations is manifested in the pressure distributions at α = 40° (figure 6(h).

Adding porosity to only the LEX weakens the LEX vortex, although there is only a minor effect on the pressure distributions at α = 15° (figure 6(b)). The diffused LEX vortex induces slightly higher maximum suction pressures at $x/c_{r,w}$ = 0.30, presumably because it is flatter and closer to the surface as it initially traverses the wing flow field. In addition, the minor suction pressure peaks situated near mid-span at $x/c_{r,w}$ = 0.60 and 0.80 provide a subtle indication of the location of the LEX vortex relative to the wing vortex. The effect of LEX porosity is more significant at α = 20° (figure 6(c)), where the wing vortex is less constrained by the deflected flap in the presence of the diffused LEX vortex. For example, the suction pressure signatures of the LEX and wing vortices are positioned inboard of the flap

hingeline at $x/c_{r,w}$ = 0.60, and the vortex signatures merge into a single suction pressure peak $x/c_{r,w}$ = 0.80. These trends are similar to those previously observed with the solid LEX and porous flap, where the inboard migration of the wing vortex was also less constrained. In contrast, the pressure distributions at $x/c_{r,w}$ = 0.60 and 0.80 on the baseline configuration indicate that direct interaction of the LEX and wing vortices has not occurred at this angle of attack. The data at α = 25° (figure 6(d)) suggest the LEX and wing vortices have combined at $x/c_{r,w}$ = 0.60 and 0.80, and the reduced overall suction pressure level at $x/c_{r,w}$ = 0.80 is consistent with the upstream influence of vortex breakdown over the wing. Similar effects are observed at α = 30° (figure 6(e)) and α = 32.5° (figure 6(f)), and the forward advance of vortex breakdown is apparent at α = 35° (figure 6(g)) and α = 40° (figure 6(h)). In general, the pressure distributions suggest earlier onset of vortex breakdown over the wing with porosity applied to the flap or the LEX compared to the baseline configuration, with this effect being more pronounced when the LEX vortex is weakened and diffused due to local surface porosity.

The deflected flap is even less effective in constraining the growth and inboard movement of the wing vortex when porosity is applied to both the LEX and flap. The wing vortex is situated inboard of the flap and combines with the LEX vortex at α = 15°, which is indicated by the single suction pressure signatures at all measurement stations in figure 6(b). The combination of the weakened and diffused LEX and wing vortices is effective in inducing pronounced suction pressure signatures at α = 20° and $x/c_{r,w}$ = 0.60 and 0.80 (figure 6(c)). This effect is not maintained, however, at higher angles of attack, as the weaker vortex system is more prone to vortex breakdown effects beginning at α = 25° (figure 6(c)). At these higher angles of attack, the character of the pressure distributions with the porous LEX and porous flap mirror those obtained with the porous LEX.

Longitudinal Aerodynamic Force and Moment Coefficients

Leading-edge flaps undeflected

Figure 7 compares the longitudinal aerodynamic force and moment coefficients obtained with all combinations of LEX and undeflected leading-edge flap porosity. The data symbols are color-coded to better discern the differences between the various configurations. The configuration with solid LEX and solid leading-edge flaps is a baseline represented by open, black circle symbols. Open green square symbols correspond to the solid LEX and porous flaps. Open red diamond symbols represent the configuration with porous LEX and solid flaps. Finally, open blue triangle symbols denote the configuration with porous LEX and porous flaps. Planview illustrations of all four configurations are also shown, where the shaded regions on the LEX and flaps denote when porosity is applied.

Porosity decreases the local lift curve slope at angles of attack generally greater than 15 degrees. The decreases in lift at a given angle of attack are caused by a weakening of the leading-edge vortices, reduction in overall suction pressure levels on the wing upper surface, and earlier onset of vortex instabilities. The most significant decreases in lift occur when porosity is applied to the LEX. The baseline configuration exhibits an abrupt discontinuity in the lift curve between α = 32.5° and 35°, where rapid forward advancement of vortex breakdown over the wing was inferred from the pressure distributions in figure 5. The configuration with porous flaps shows an initial discontinuity in the lift curve between α = 30° and 32.5°, where breakdown of the dominant LEX vortex and weaker wing vortex was observed in the pressure distributions (figure 5). The subsequent partial recovery of the vortex-induced suction pressures between α = 32.5° and 35° in figure 5 is consistent with a second lift curve slope discontinuity. This is followed by another drop-off in the lift coefficient beyond α = 35° as vortex breakdown continues its forward advancement over the wing. The configuration with porous LEX displays a discontinuity in the

local lift curve slope between α = 22.5° and 25°, where the effects of breakdown of the wing vortex-dominated flow field were suggested in the pressure distributions at α = 25° in figure 5. It is speculated that the forward advance of vortex breakdown is more gradual with the weaker combined LEX and wing vortex system compared to the baseline configuration, such that the lift curve slope remains positive until vortex breakdown advances more rapidly over the wing at angles of attack beyond 35°. The greatest loss in lift is observed when porosity is applied to both the LEX and flaps. Similar to the porous LEX configuration, it is speculated that the weaker LEX and wing vortices exhibit early breakdown and a less rapid forward advancement up to angles of attack of 32.5°, beyond which vortex breakdown marches forward more rapidly over the wing.

Porosity significantly increases the drag-due-to-lift, and the effect is most pronounced when porosity is applied to the LEX. All configurations with surface porosity generate lift less efficiently than the baseline configuration. Consequently, higher angles of attack are required in order to achieve the same lift levels. An additional source of drag is attributed to the flow through the array of 0.050-inch-diameter holes in the porous surfaces.

The application of porosity to the LEX and flaps promotes small nose-down pitching moment coefficient increments at a given lift coefficient at angles of attack below the onset of vortex breakdown. However, the reduction in the static longitudinal stability level relative to the baseline configuration is insignificant.

Leading-edge flaps deflected 30 degrees

Figure 8 compares the longitudinal aerodynamic force and moment coefficients obtained with all combinations of LEX and deflected leading-edge flap porosity. The data symbols are color-coded in the same manner as the previous section with the undeflected leading-edge flaps to better discern the differences between the various configurations.

The pressure distributions previously shown in figure 6 suggested that deflection of the leading-edge flap on the baseline configuration constrained the growth and inboard movement of the wing vortex and reduced the direct interaction of the LEX and wing vortices. A primary outcome of the application of porosity to the LEX and flaps is also the modulation of the LEX and wing vortex interactions. Consequently, the quantitative effects of porosity on the lift coefficient are more conservative when the leading-edge flaps are deflected to 30 degrees (figure 8). The lift curve obtained with the porous flaps tracks along the baseline configuration lift curve, except at angles of attack from 30° to 35°, where C_L discontinuities occur similar to those observed with the undeflected porous flaps in figure 7. The onset of a lift coefficient decrease due to the application of porosity to the LEX is delayed to a higher angle of attack compared to the configuration with undeflected flaps, and the lift coefficient decrements are less once they occur. Similar trends are observed when porosity is applied to the LEX and flaps. The latter configuration also exhibits lift curve discontinuities at angles of attack below maximum lift that may also be related to asymmetries in the interactions of the interacting, weaker LEX and wing vortices.

The effect of porosity on the drag-due-to-lift is similar to that described in the previous section for the configuration with undeflected leading-edge flaps. The drag coefficient increase due to porosity at a given lift coefficient is generally reduced with the flaps deflected.

The delay to higher angles of attack of the onset of lift decrements due to porosity is consistent with a reduction in the static longitudinal instability through the corresponding range of lift coefficient. This is particularly the case for the configurations with porosity applied to the LEX. The more significant effects on the pitching moment coefficient with the porous LEX configurations subsequently diminish as these

configurations become less efficient at the higher levels of lift coefficient.

Static Lateral-Directional Stability Derivatives

Leading-edge flaps undeflected

Figure 9 compares the static lateral-directional stability derivatives obtained in angle-of-attack sweeps with all combinations of LEX and undeflected leading-edge flap porosity. The data symbols are color-coded to better discern the differences between the various configurations. The configuration with solid LEX and solid leading-edge flaps is a baseline represented by open, black circle symbols. Open green square symbols correspond to the solid LEX and porous flaps. Open red diamond symbols represent the configuration with porous LEX and solid flaps. Finally, open blue triangle symbols denote the configuration with porous LEX and porous flaps. Planview illustrations of all four configurations are also shown, where the shaded regions on the LEX and flaps denote when porosity is applied.

The baseline configuration exhibits an unstable break in the lateral stability at an angle of attack of approximately 18 degrees due to early onset of LEX and wing vortex breakdown over the windward wing surface compared to the leeward wing surface (reference 8). The static lateral stability of the baseline configuration continues to decrease until it becomes slightly unstable in roll around α = 30°. This trend is associated with the increasing vortex breakdown asymmetry between the windward and leeward wing surfaces. At higher angles of attack, vortex breakdown occurs over the leeward wing surface, and the diminished flow asymmetries result in a recovery of the static lateral stability. The onset of vortex breakdown over the windward wing surface also promotes an unstable break in the directional stability, followed by directional instability at the higher angles of attack. This trend is attributed to the decrease in the local dynamic pressure environment at the centerline vertical tail as a result of the lower-energy wake associated with windward LEX and wing vortex breakdown.

Applying porosity to the undeflected flaps slightly delays the onset of the unstable breaks in the lateral and directional stability but, otherwise, has an insignificant effect on the stability derivatives throughout the range of angle of attack.

In contrast, weakening the LEX vortex by applying surface porosity has a significant adverse effect on the lateral-directional stability characteristics. Both configurations with porous LEX exhibit unstable breaks in the lateral and directional stability at angles of attack of approximately 10° to 12° and are highly unstable in roll and yaw at the higher angles of attack. The windward wing surface is more prone to early vortex breakdown and a more rapid progression of breakdown in the presence of the weaker LEX vortex.

Leading-edge flaps deflected 30 degrees

Figure 10 compares the static lateral-directional stability derivatives obtained in angle-of-attack sweeps with all combinations of LEX and deflected leading-edge flap porosity. The data symbols are color-coded in the same manner as the previous section with the undeflected leading-edge flaps to better discern the differences between the various configurations.

The abrupt discontinuities in the lateral-directional stability derivatives that were observed on the baseline configuration with undeflected flaps in figure 9 beginning at an angle of attack of approximately 18° are delayed to nearly 28° with the flaps deflected to 30°. This trend is attributed to a delay in the progression of vortex breakdown over the windward wing. At higher angles of attack where vortex breakdown effects are dominant, the lateral-directional stability characteristics with deflected flaps are similar to those previously observed with undeflected flaps.

All configurations with porosity display degraded lateral-directional stability characteristics compared to the baseline

configuration. This is particularly the case for the two configurations featuring porous LEX. The mitigating effect of the deflected flaps on the stability derivatives is less significant in the presence of the porous surfaces. In general, the application of porosity to the LEX or flaps weakens the leading-edge vortices, rendering them more susceptible to asymmetric breakdown in sideslip conditions.

Concluding Remarks

A wind tunnel experiment was conducted in the NASA LaRC 7- by 10-Foot HST to determine the effects of passive surface porosity on the subsonic vortex flow interactions about a general research fighter configuration. Flow-through porosity was applied to the LEX and leading-edge flaps mounted to a 65° cropped delta wing model as a potential vortex flow control technique at high angles of attack. All combinations of nonporous (solid) and porous LEX and flaps were investigated. Wing upper surface static pressure distributions and six-component forces and moments were obtained at a free-stream Mach number of 0.20 corresponding to a Reynolds number of $1.35(10^6)$ per foot, angles of attack from -2.5° to 45°, angles of sideslip of 0° and +/-5°, and leading-edge flap deflections of 0° and 30°. The configuration with nonporous surfaces represented a balance between the LEX and wing vortices, which exhibited a highly-interactive and synergistic effect at high angles of attack. The application of flow-through porosity to the LEX or wing leading-edge flaps was a vorticity-limiting mechanism that altered the relative strengths of the LEX and wing vortices and the manner in which these vortices interacted at high angles of attack. Porous flaps weakened the wing vortices and produced a flow field that was dominated by the LEX vortex. Conversely, the porous LEX resulted in a wing vortex-dominated flow field. Porosity applied to both the LEX and flaps yielded a flow field characterized by weaker interacting vortices. The effects of passive porosity were reduced in the presence of deflected wing flaps, since the leading-edge devices also affected the relative strengths of the vortex flows. Application of passive porosity typically decreased the vortex-induced lift, increased the drag, and produced relatively small effects on the longitudinal stability characteristics. In addition, porosity had an adverse effect on the static lateral-directional stability derivatives, since the porous configurations were more susceptible to a more rapid advance of asymmetric vortex breakdown in sideslip conditions. The most significant effects on the longitudinal and lateral-directional aerodynamic and stability characteristics occurred when porosity was applied to the LEX.

References

1. Frink, N. T.: *Concept for Designing Vortex Flap Geometries*. NASA TP-2233, 1983.

2. Bauer, S. X. S. and Hemsch, M. J.: *Alleviation of Side Force on Tangent-Ogive Forebodies Using Passive Porosity*. AIAA-92-2711, June 1992.

3. Bauer, S. X. S. and Hernandez, G.: *Reduction to Cross-Flow Shock-Induced Separation with a Porous Cavity at Supersonic Speeds*. AIAA-88-2567, June 1988.

4. Elsenaar, A.: How It All Started: *The International Vortex Flow Experiment on Euler Code Validation in Retrospect*. Symposium on International Vortex Flow Experiment on Euler Code Validation – Proceedings, A. Elsenaar and G. Eriksson, eds., FFA, Flygtekniska Försöksanstalten (Sweden), Oct. 1986, pp. 17-19.

5. Erickson, G. E.: *Wind Tunnel Investigation of the Interaction and Breakdown Characteristics of Slender-Wing Vortices at*

Subsonic, Transonic, and Supersonic Speeds. NASA TP 3114, 1991.

6. Erickson, G. E. and Inenaga, A. S.: *Fiber-Optic-Based Laser Vapor Screen Flow Visualization for Aerodynamic Research in Larger Scale Subsonic and Transonic Wind Tunnels*. NASA TM 4514, 1994.

7. Erickson, G. E.: *Wind Tunnel Investigation of the Effects of Surface Porosity and Vertical Tail Placement on Slender Wing Vortex Flow Aerodynamics at Supersonic Speeds.* NASA TM-2007-215082, October 2007.

8. Erickson, G. E.: *Wind Tunnel Investigation of Passive Vortex Control and Vortex-Tail Interactions on a Slender Wing at Subsonic and Transonic Speeds*. NASA TM-2013-217982, 2013.

9. Braslow, A. L., Hicks, R. M., and Harris, R. V., Jr.: *Use of Grit-Type Boundary-Layer Transition Strips on Wind-Tunnel Models*. NASA TN D-3579, 1966.

10. Hall, R. M., Erickson, G. E., and Fox, C. H., Jr.: *Evaluation of Gritting Strategies for High Angle of Attack Using Wind Tunnel and Flight Test Data for the F/A-18.* NASA TP-1998-207670, May 1998.

11. Fox, C. H., Jr. and Huffman, J. K.: *Calibration and Test Capabilities of the Langley 7- by 10-Foot High Speed Tunnel.* NASA TM X-74027, 1977.

12. Gillis, C. L., Polhamus, E. C., and Gray, J. L., Jr.: *Charts for Determining Jet-Boundary Corrections for Complete Models in the 7- by 10-Foot Closed Rectangular Wind Tunnels.* NACA WR L-123, 1945.

13. Herriot, J. G.: *Blockage Corrections for Three-Dimensional Flow Closed-Throat Wind Tunnels, With Consideration of the Effect of Compressibility.* NASA Rep. 995, 1950. (Supersedes NACA RM A7B28.)

14. A. B. Graham.: *Data Engineering Scripting Language (DESL)*, ViGYAN, Inc.

15. Erickson, G. E., Peake, D. J., Del Frate, J., Skow, A. M., and Malcolm, G. N.: *Water Facilities in Retrospect and Prospect—an Illuminating Tool for Vehicle Design.* NASA TM-89409, 1986.

Table I. 65° cropped delta wing model geometry details.

Model Geometry Details							
Wing		*LEX*		*Centerline Tail*		*Leading-Edge Flaps*	
Airfoil	Modified NACA 64A005 with sharp leading edge	*Airfoil*	Flat plate with symmetrically-beveled leading edge	*Airfoil*	Flat plate with symmetrically-beveled leading edge	*Airfoil*	Flat plate with symmetrically-beveled leading edge
$\Lambda_{LE,w}$	65°	$\Lambda_{LE,lex}$	65°	$\Lambda_{LE,cl}$	45°	$\Lambda_{LE,\,flap}$	30°/65°
$\Lambda_{TE,w}$	0°	$\Lambda_{TE,lex}$	65°	$\Lambda_{TE,cl}$	70°		
$c_{r,w}$	23.622 in.	$c_{r,lex}$	7.680 in.	$c_{r,cl}$	6.881 in.		
$c_{t,w}$	3.544 in.	$c_{t,lex}$	7.680 in.	$c_{t,cl}$	3.175 in.		
b_w	18.726 in.	b_{lex}	4.960 in.	b_{cl}	5.829 in.		
$\bar{c}_w$	16.056 in.	$\bar{c}_{lex}$	7.680 in.	$\bar{c}_{cl}$	5.256 in.		
λ_w	0.150	λ_{lex}	1.000	λ_{cl}	0.461		
S_w	254.3553 in.^{2} (1.7664 ft.^{2})	S_{lex}	38.0928 in.^{2} (0.2645 ft.^{2})	S_{cl}	29.308 in.^{2} (0.2035 ft.^{2})	S_{flap}	15.244 in.^{2} (0.1059 ft.^{2}) (per flap)
MRC	$0.57\,c_{r,w}$ (M.S. 21.144)			$l_{0.25\bar{c}_{cl}}$	8.647 in. (M.S. 29.791)		
S_{cham}	4.909 in.^{2} (0.03409 ft.^{2})			V_{cl}	253.4398 in.^{3} (0.1467 ft.^{3})		

Table II. 65° cropped delta wing model pressure orifice locations.

Pressure Orifice Locations											
MS (in.)	$x/c_{r,w}$	*y (in.)*	*y/s*	*MS (in.)*	$x/c_{r,w}$	*y (in.)*	*y/s*	*MS (in.)*	$x/c_{r,w}$	*y (in.)*	*y/s*
14.767	0.30	0.000	0.00	21.853	0.60	0.661	0.10	26.578	0.80	1.762	0.20
↓	↓	0.331	0.10	↓	↓	1.322	0.20	↓	↓	3.525	0.40
		0.661	0.20			1.983	0.30			4.406	0.50
		0.992	0.30			3.304	0.50			4.847	0.55
		1.322	0.40			3.635	0.55			5.287	0.60
		1.652	0.50			3.965	0.60			5.728	0.65
		1.818	0.55			4.626	0.70			5.948	0.675
		1.983	0.60			4.792	0.725			6.168	0.70
		2.066	0.625			4.957	0.75			6.389	0.725
		2.148	0.65			5.122	0.775			6.829	0.775
		2.231	0.675			5.287	0.80			7.270	0.825
		2.314	0.70			5.452	0.825			7.490	0.85
		2.396	0.725			5.618	0.85			7.711	0.875
		2.479	0.75			5.948	0.90			7.931	0.90
		2.727	0.825			6.080	0.92				
		2.809	0.85								
		2.892	0.875								
		2.974	0.90								

Table III. NASA LaRC 842A balance design loads and calibration accuracies (95% confidence limits (CL) about the mean response).

Component	*Design Load (lbs or in-lbs)*	*Full Scale Output (mV)*	*Accuracy % F.S. (95% CL)*	*Accuracy (μV) (95% CL)*	*Accuracy (lbs or in-lbs) (95% CL)*
Normal Force	±1600	9.350	0.09	8.42	1.44
Axial Force	75	5.920	0.40	23.68	0.30
Pitching Moment	±3000	7.255	0.10	7.26	3.00
Rolling Moment	±1500	7.490	0.10	7.49	1.50
Yawing Moment	±1500	6.630	0.17	11.27	2.55
Side Force	±500	5.395	0.19	10.25	0.95

Table IV. 842A balance calibration accuracies expressed in terms of aerodynamic force and moment coefficients.

Mach	q_∞, *psf*	C_N	C_A	C_m	C_l	C_n	C_Y
0.20	58	±0.0141	±0.0029	±0.0012	±0.0008	±0.0013	±0.0093

Table V. ESP measurement uncertainties for 7- by 10-Foot HST Test 220 expressed in terms of the static pressure coefficient (95% confidence limits about the mean response).

Mach	q_∞ (psf)	C_p *uncertainty,* ΔC_p *(95% CL)*
0.20	58	±0.0186

$$\Delta C_p = \frac{\Delta p}{q_\infty} = \frac{0.0005 * 15 \text{ psi} * 144 \text{ sq.in / sq. ft.}}{q_\infty} = \frac{1.08 \text{ psf}}{q_\infty}$$

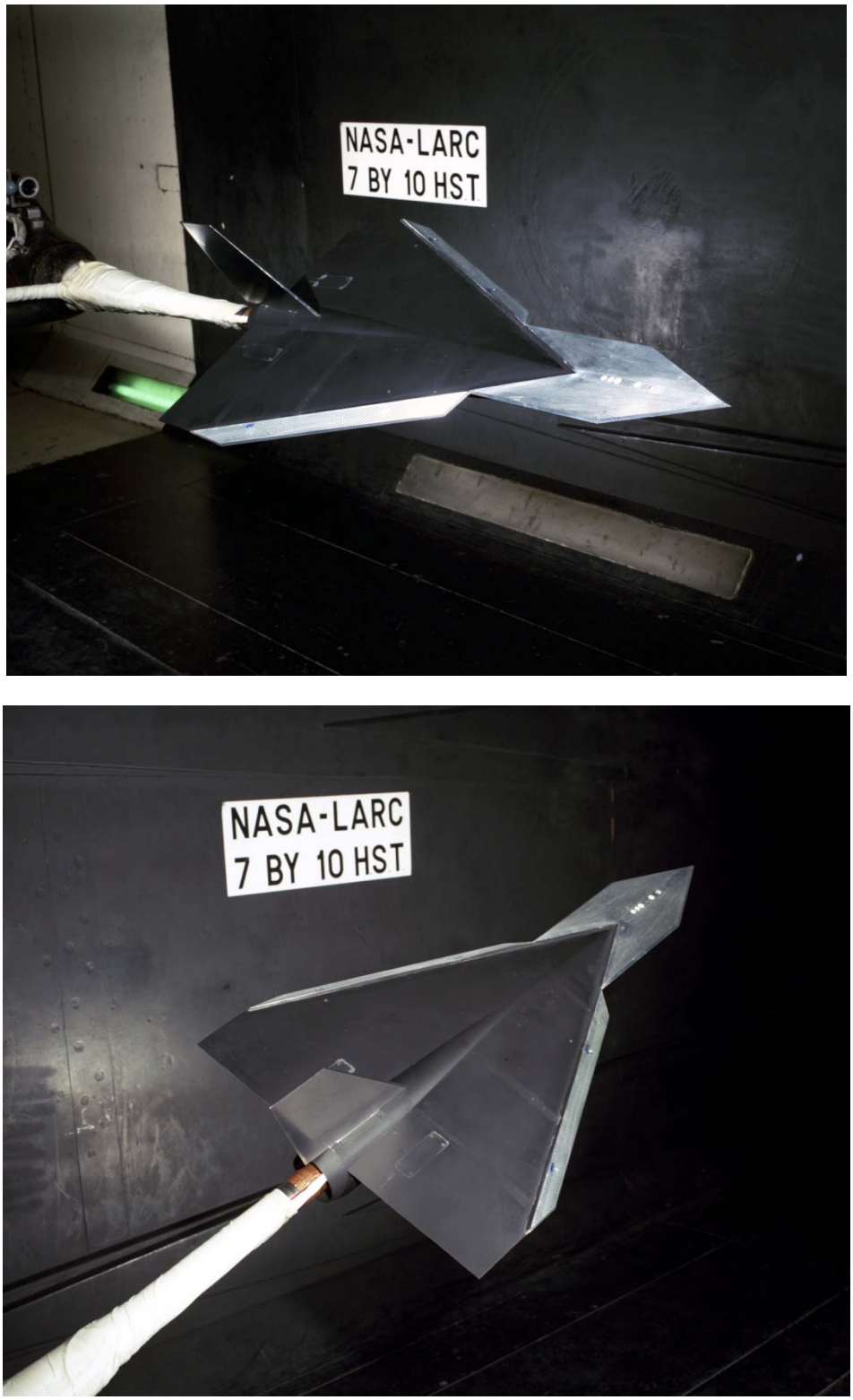

Figure 1. Photographs of the 65° cropped delta wing model installed in the NASA Langley 7- by 10-Foot High Speed Tunnel. (Porous LEX and leading-edge flaps are unpainted surfaces.)

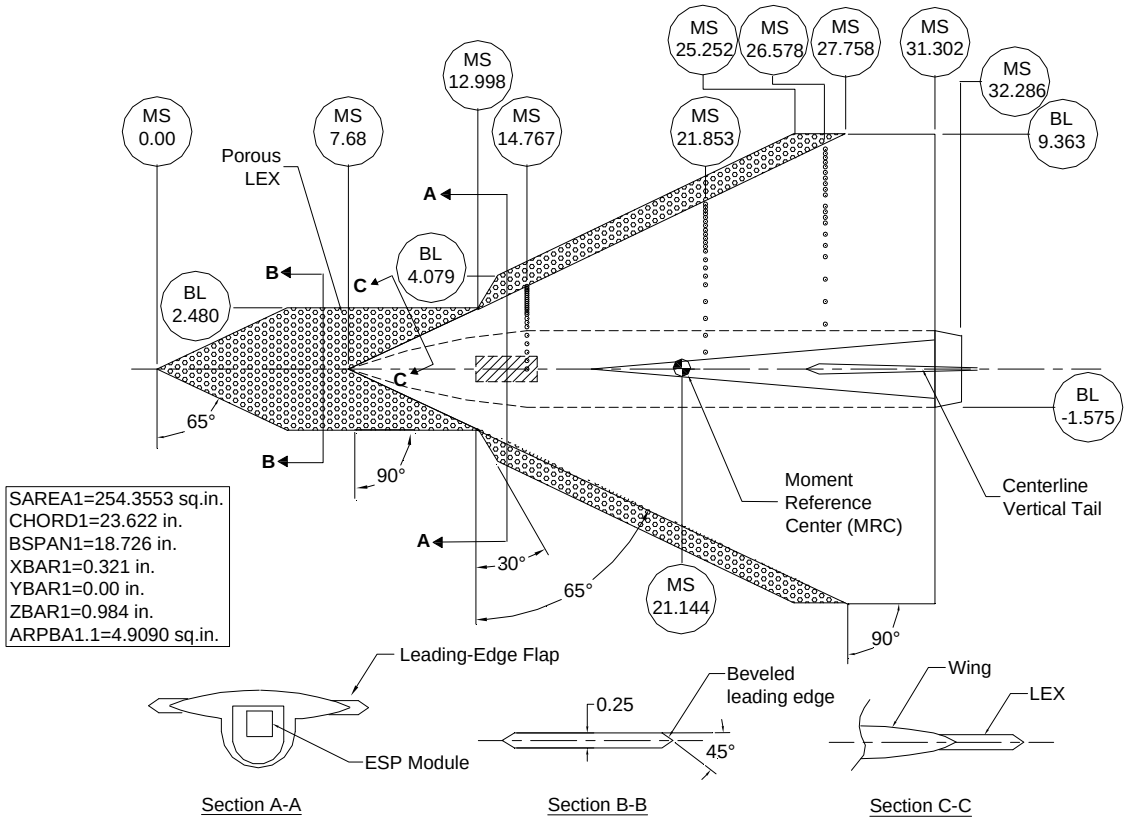

Figure 2. Planview of the 65º cropped delta wing model. (Dimensions are in inches.)

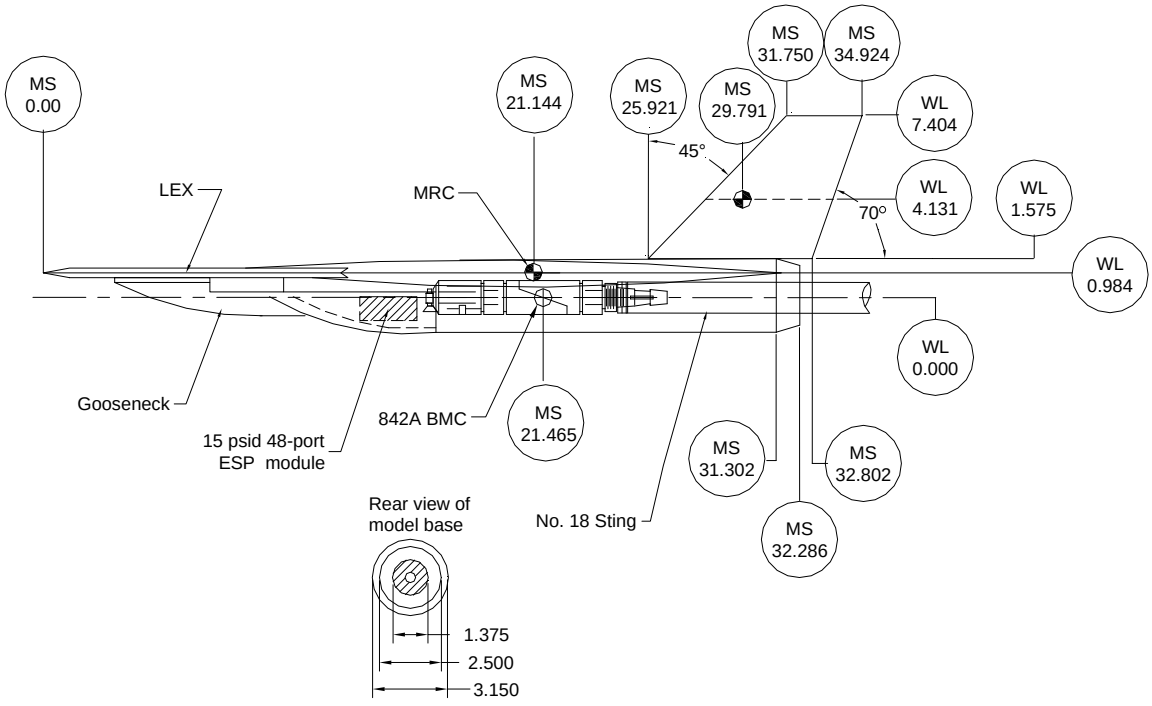

Figure 3. Sideview of the 65º cropped delta wing. (Dimensions are in inches.)

Solid LEX

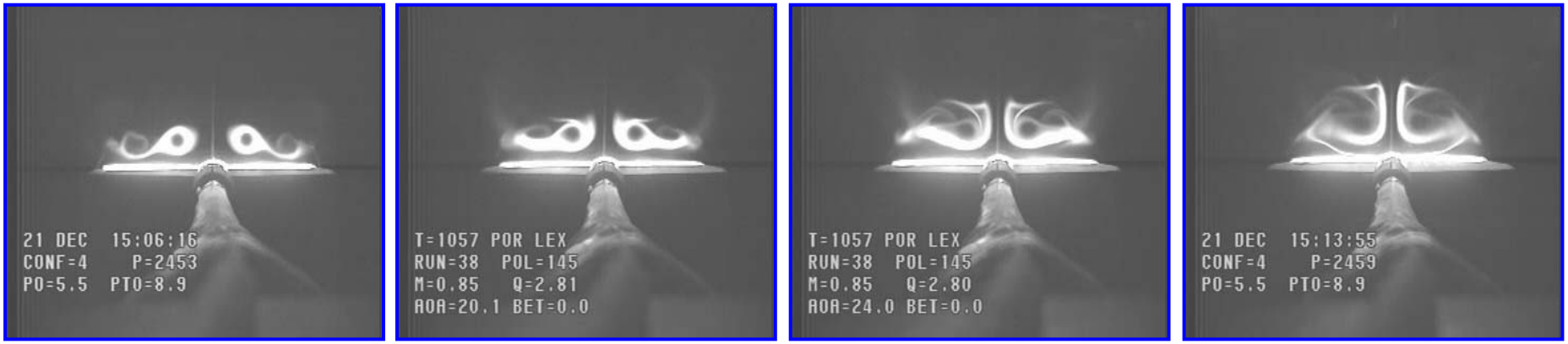

Porous LEX

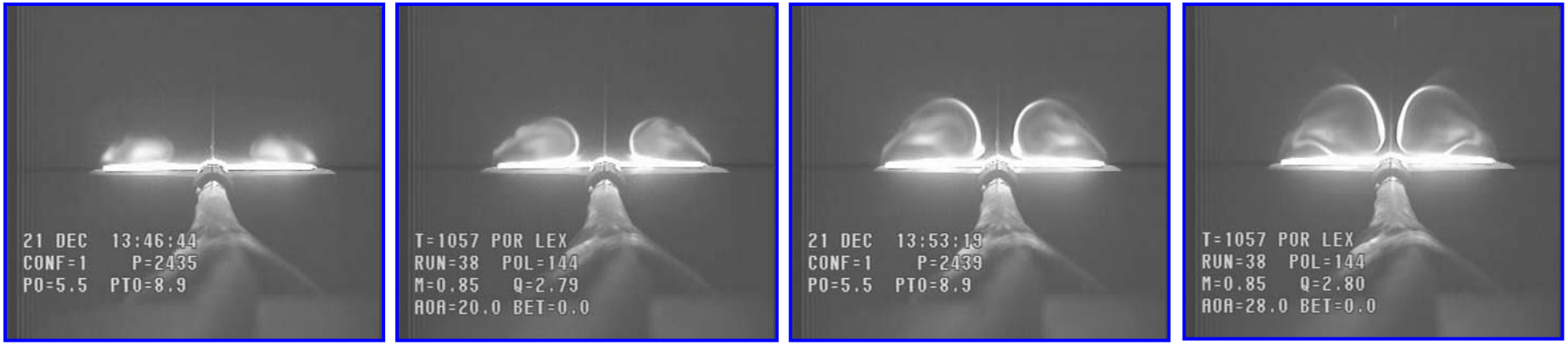

α = 16° ***α = 20°*** ***α = 24°*** ***α = 28°***

Figure 4. Laser vapor screen images of the 65° cropped delta wing model with solid LEX and porous LEX at Mach =0.85 and $x/c_{r,w}$ = 0.80 (from reference 8).

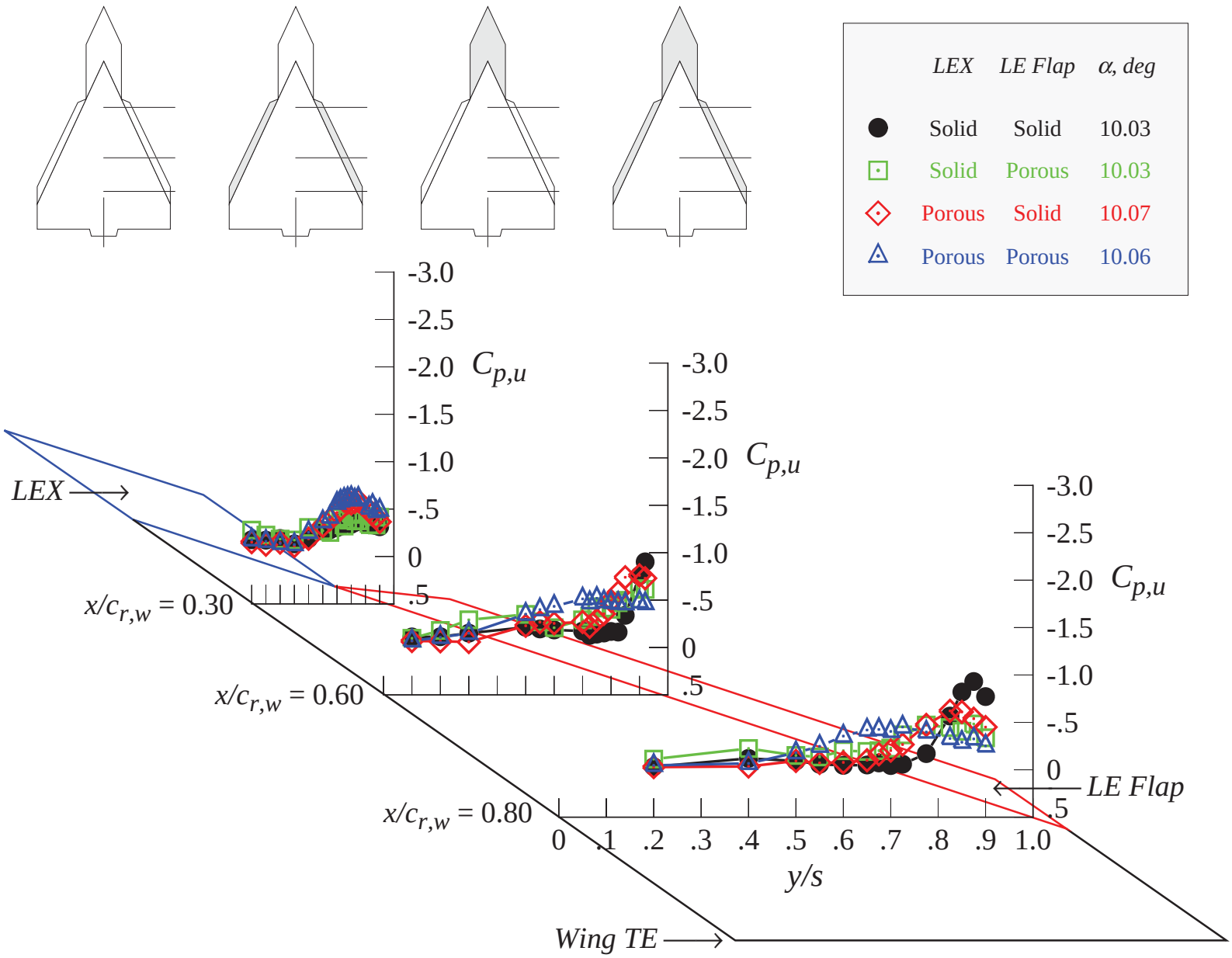

(a) α = 10°

Figure 5. Effect of porosity on the wing upper surface static pressure distributions; leading-edge flaps undeflected.

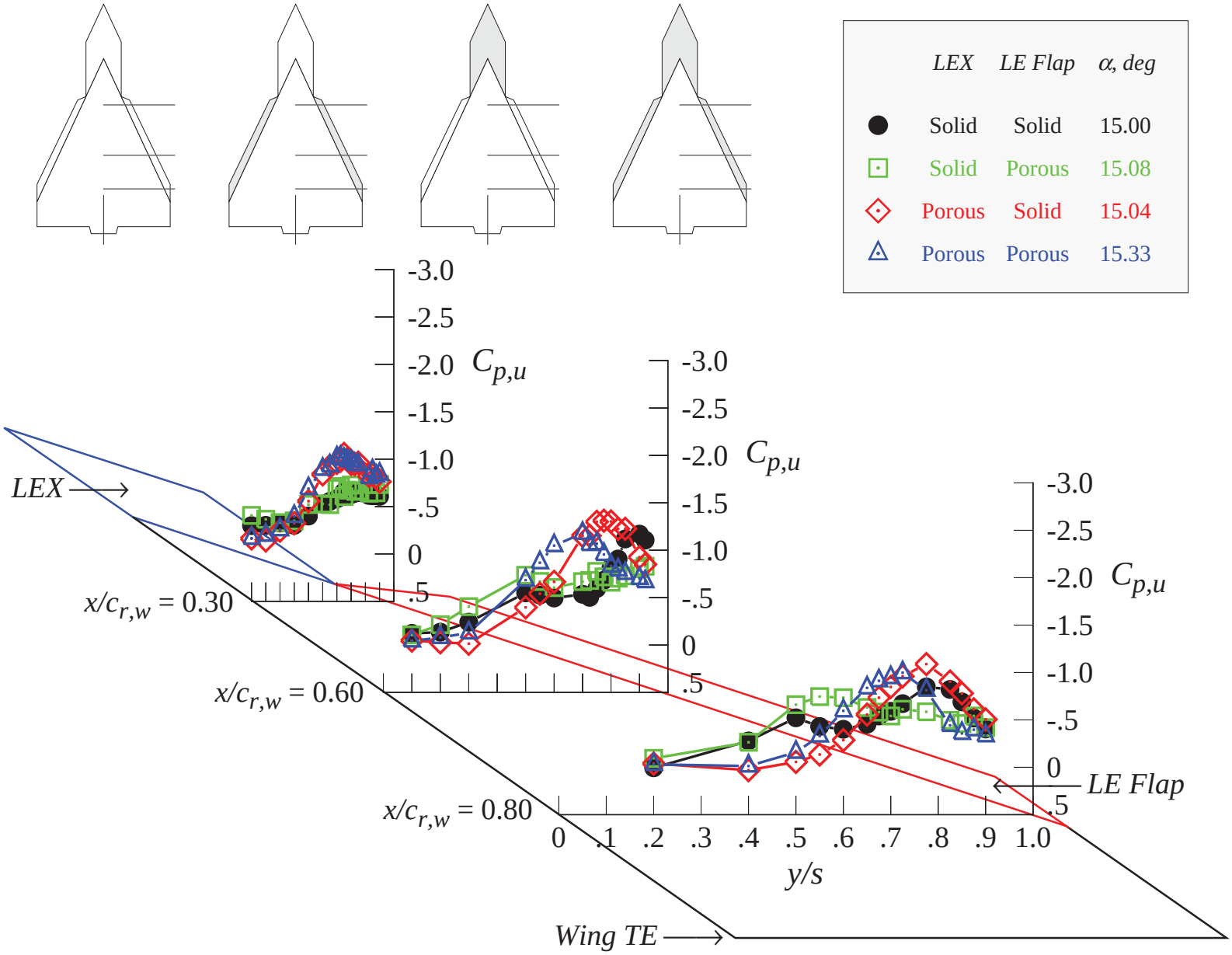

(b) α = 15°

Figure 5. Continued.

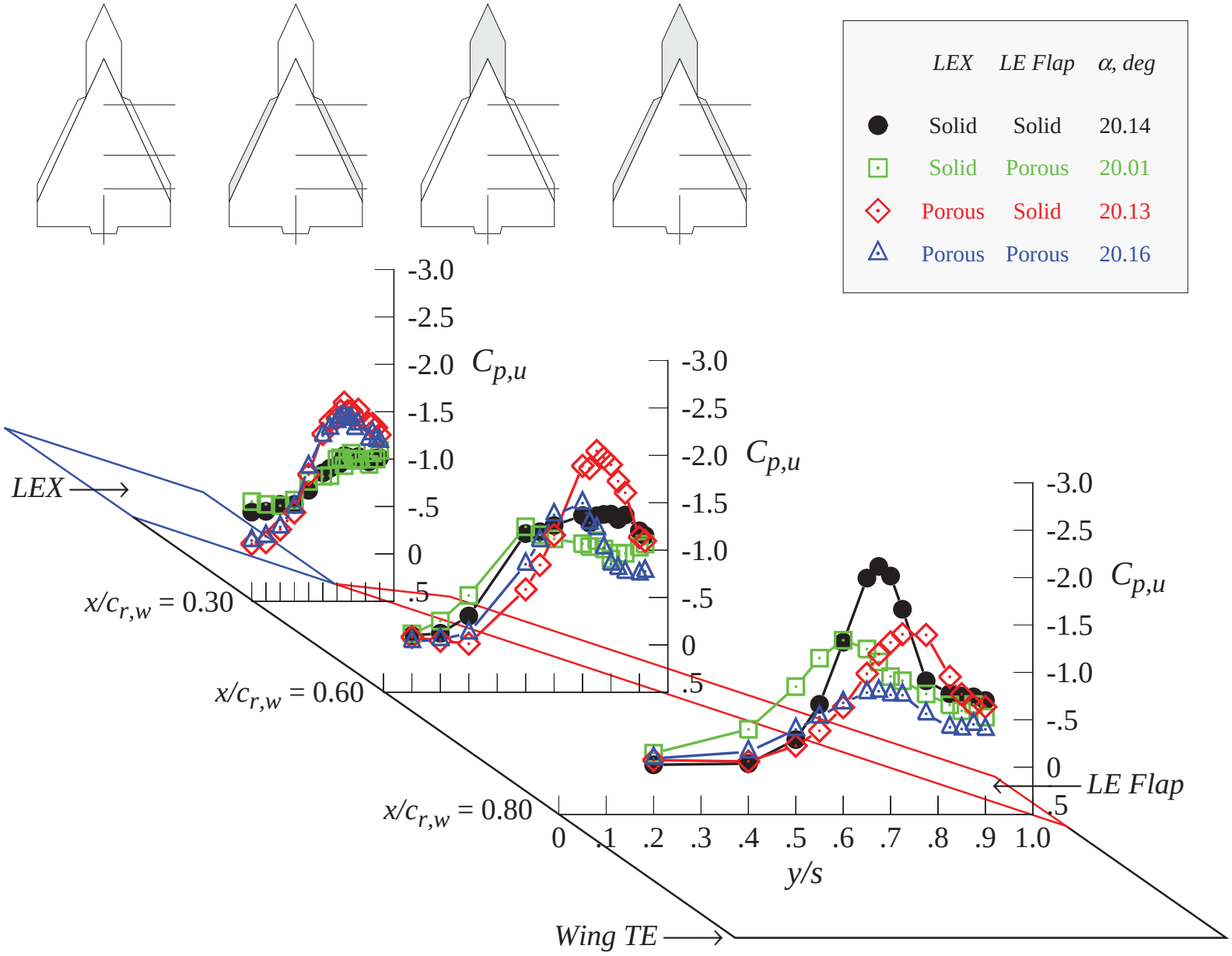

(c) α = 20°

Figure 5. Continued.

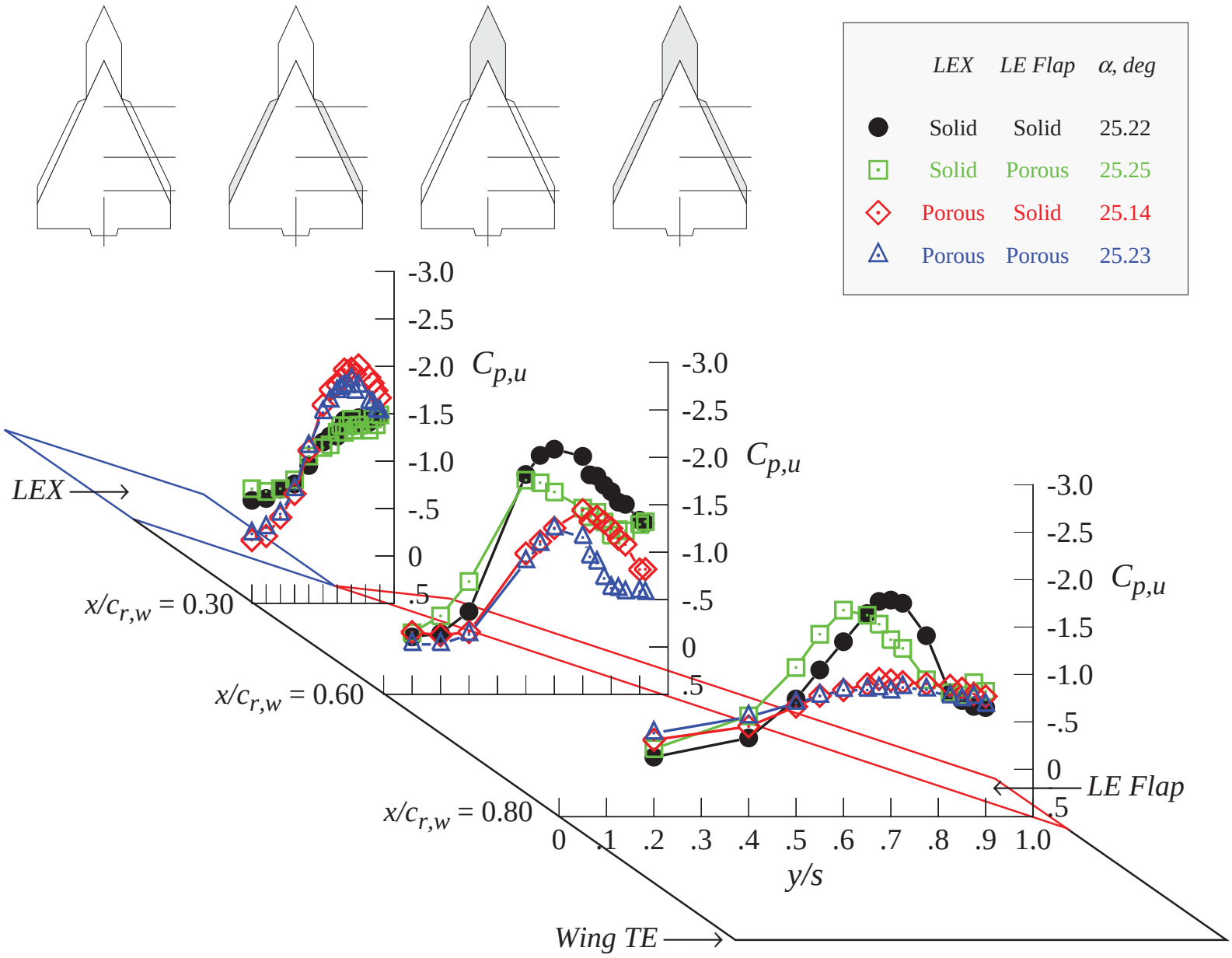

(d) α = 25°

Figure 5. Continued.

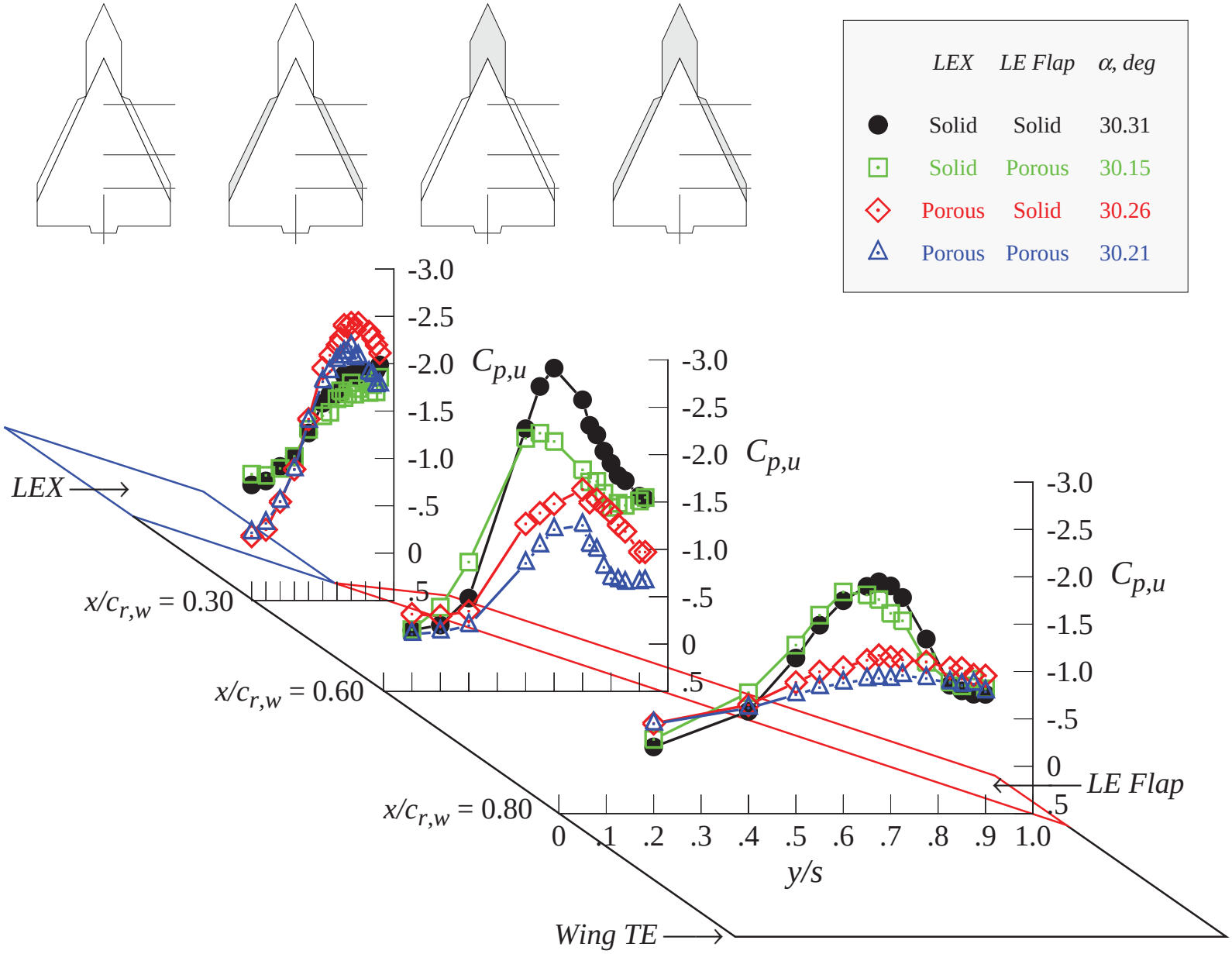

(e) α = 30°

Figure 5. Continued.

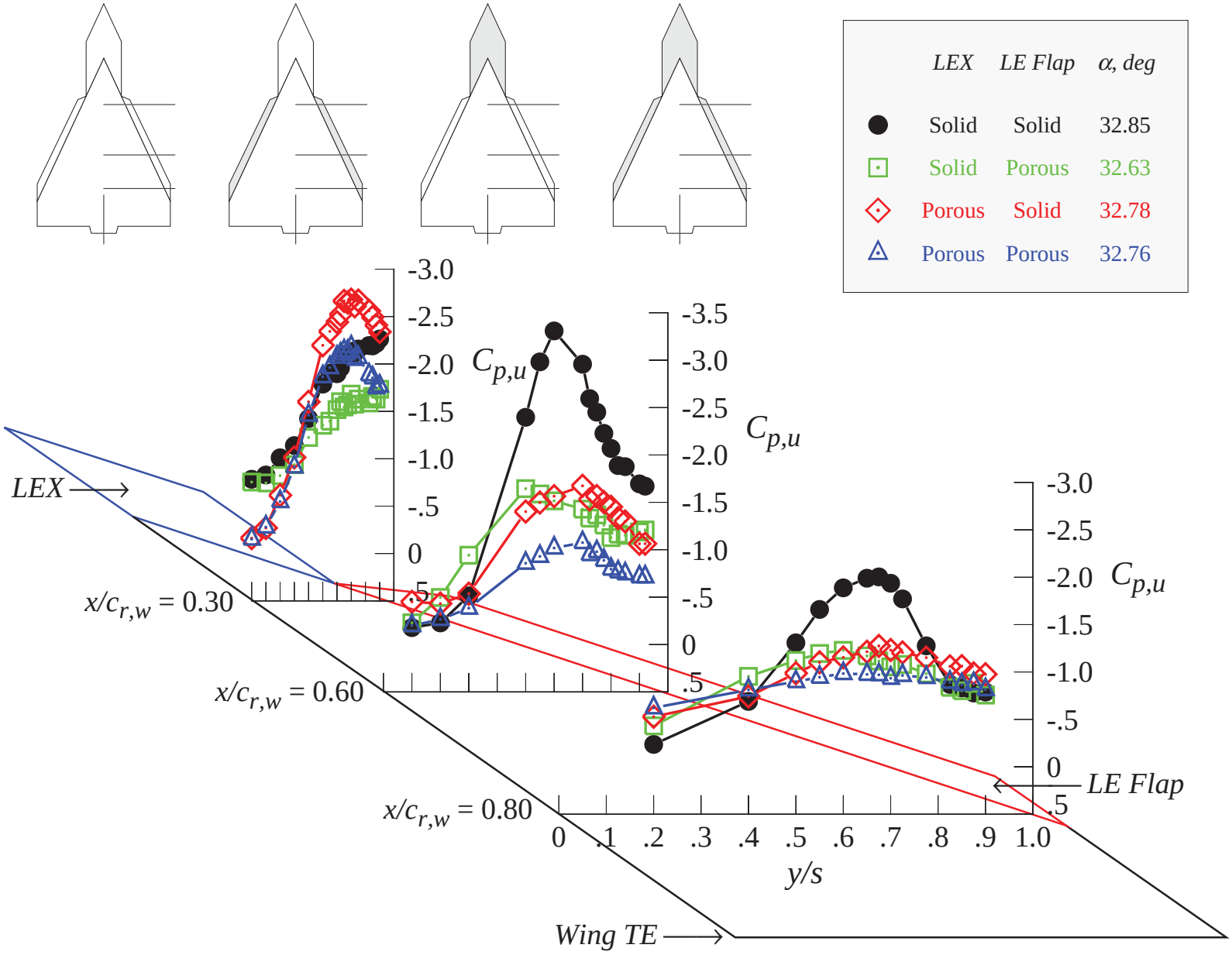

(f) α = 32.5°

Figure 5. Continued.

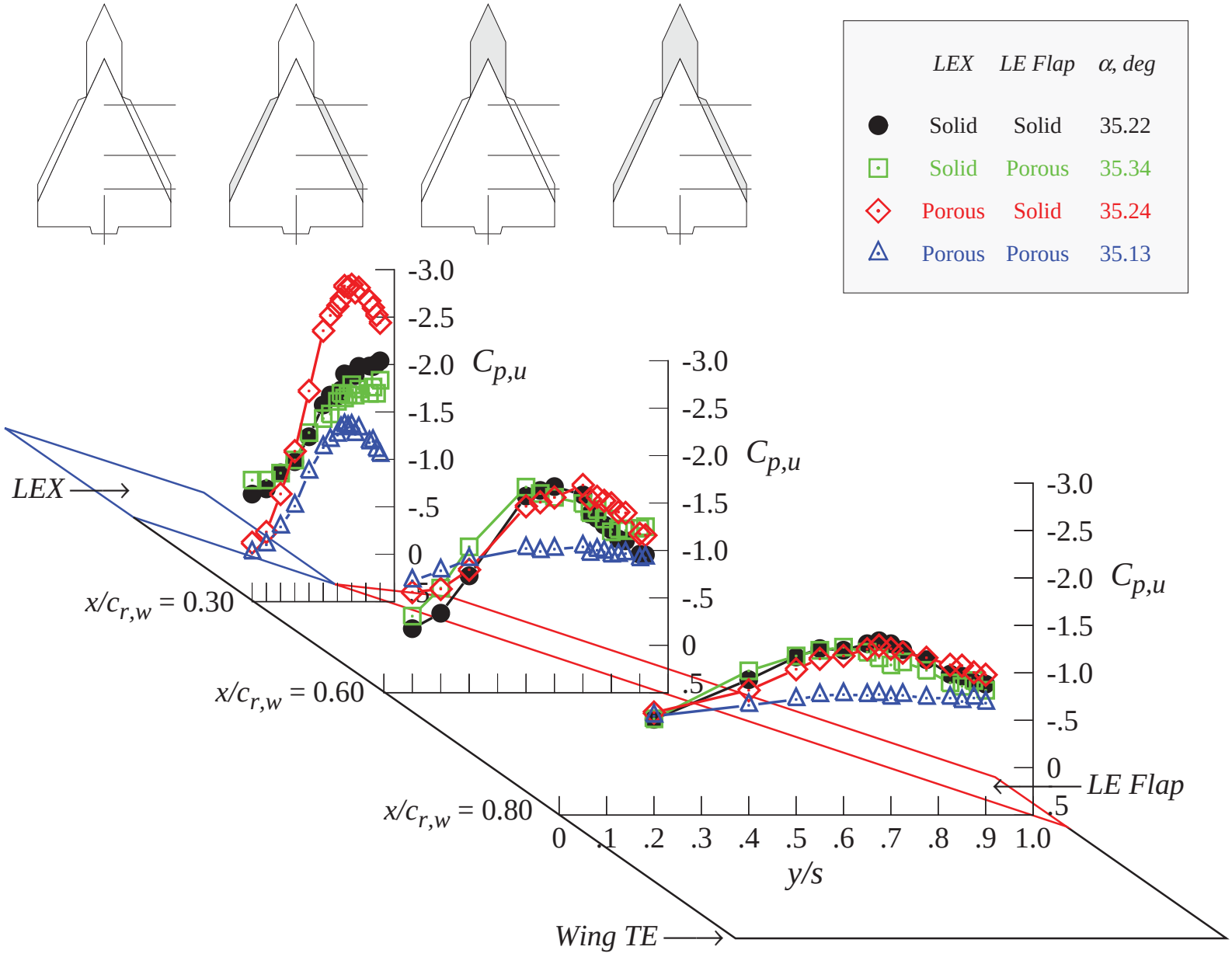

(g) α = 35°

Figure 5. Continued.

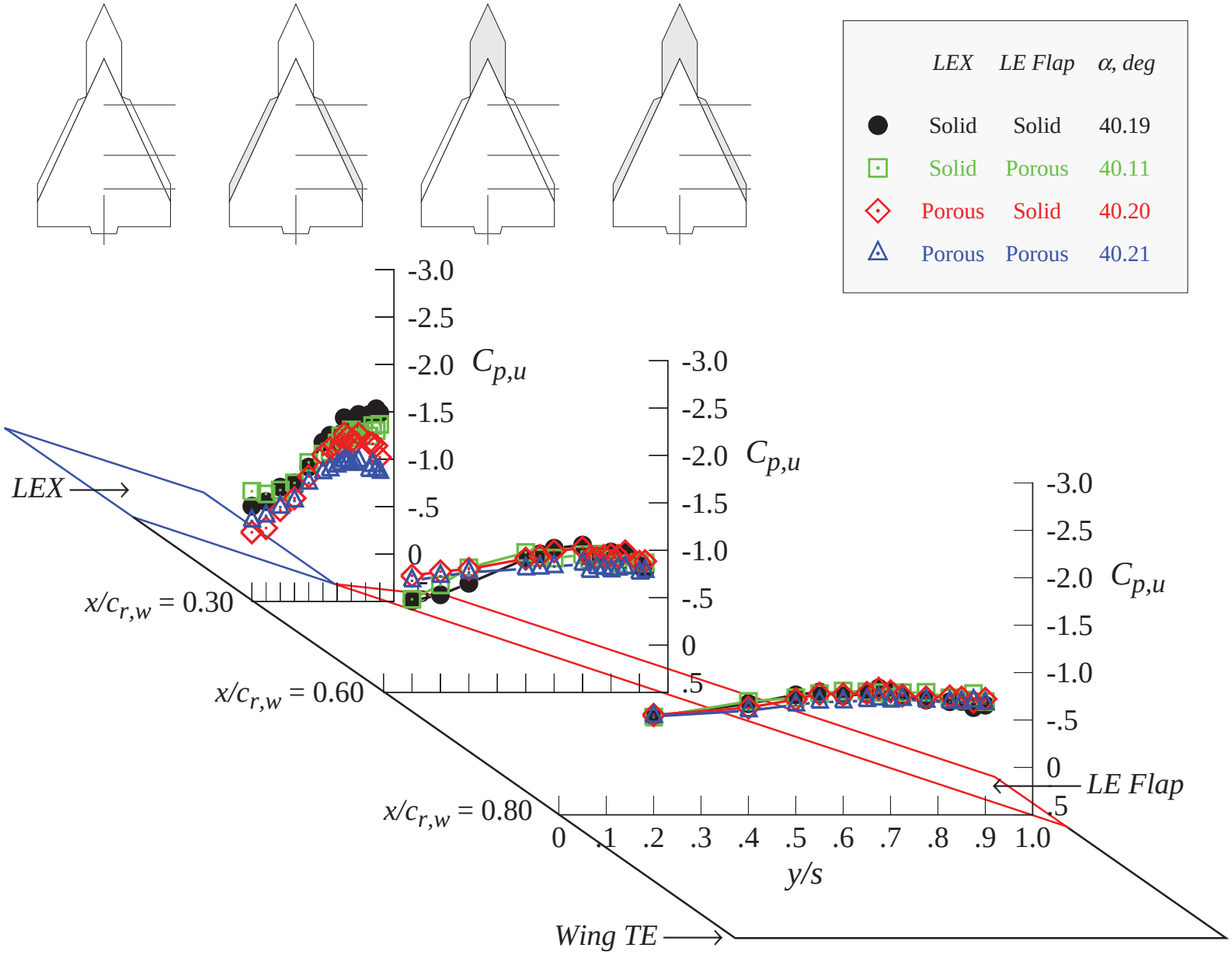

(h) α = 40°

Figure 5. Concluded.

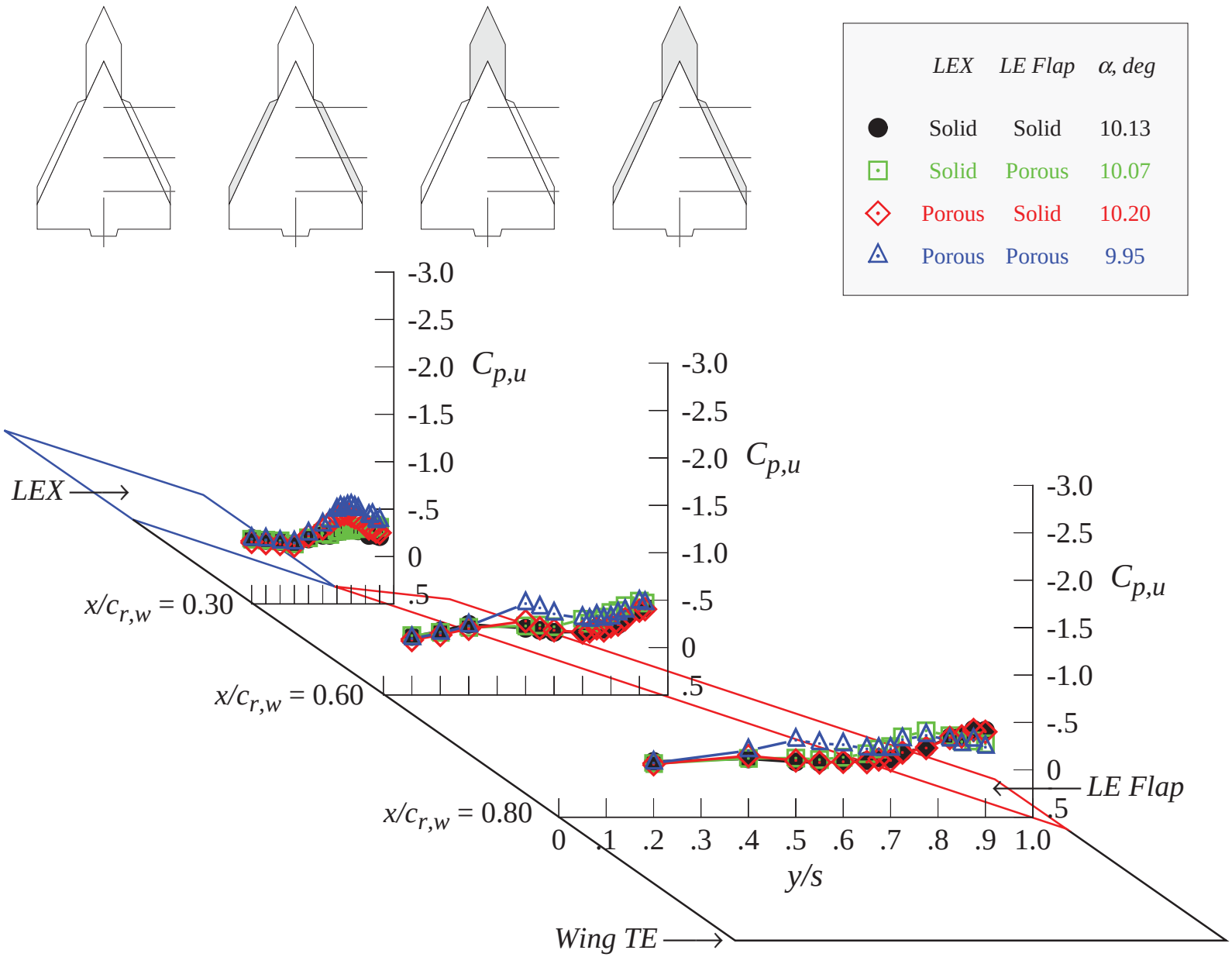

(a) α = 10°

Figure 6. Effect of porosity on the wing upper surface static pressure distributions; leading-edge flaps deflected 30°.

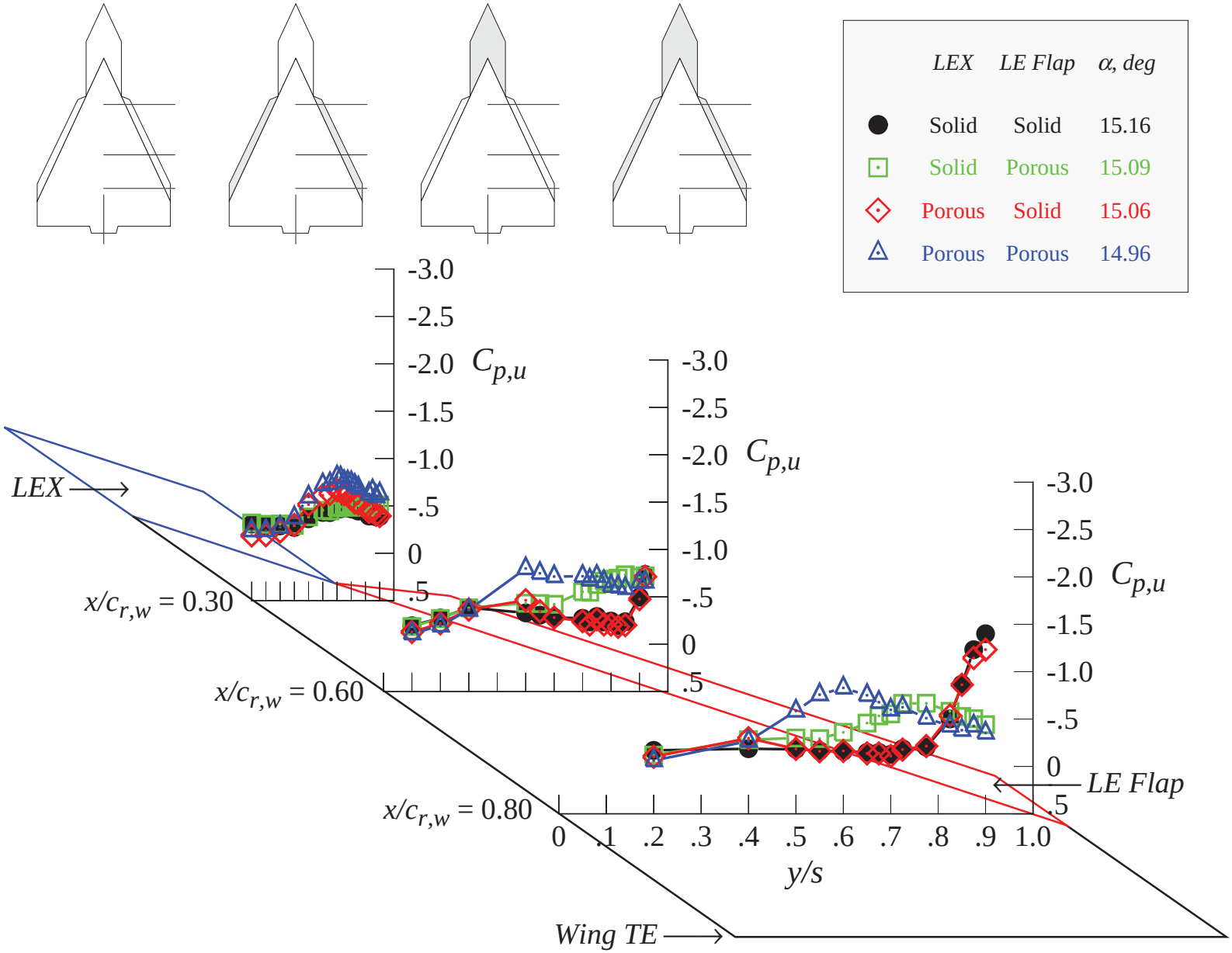

(b) α = 15°

Figure 6. Continued.

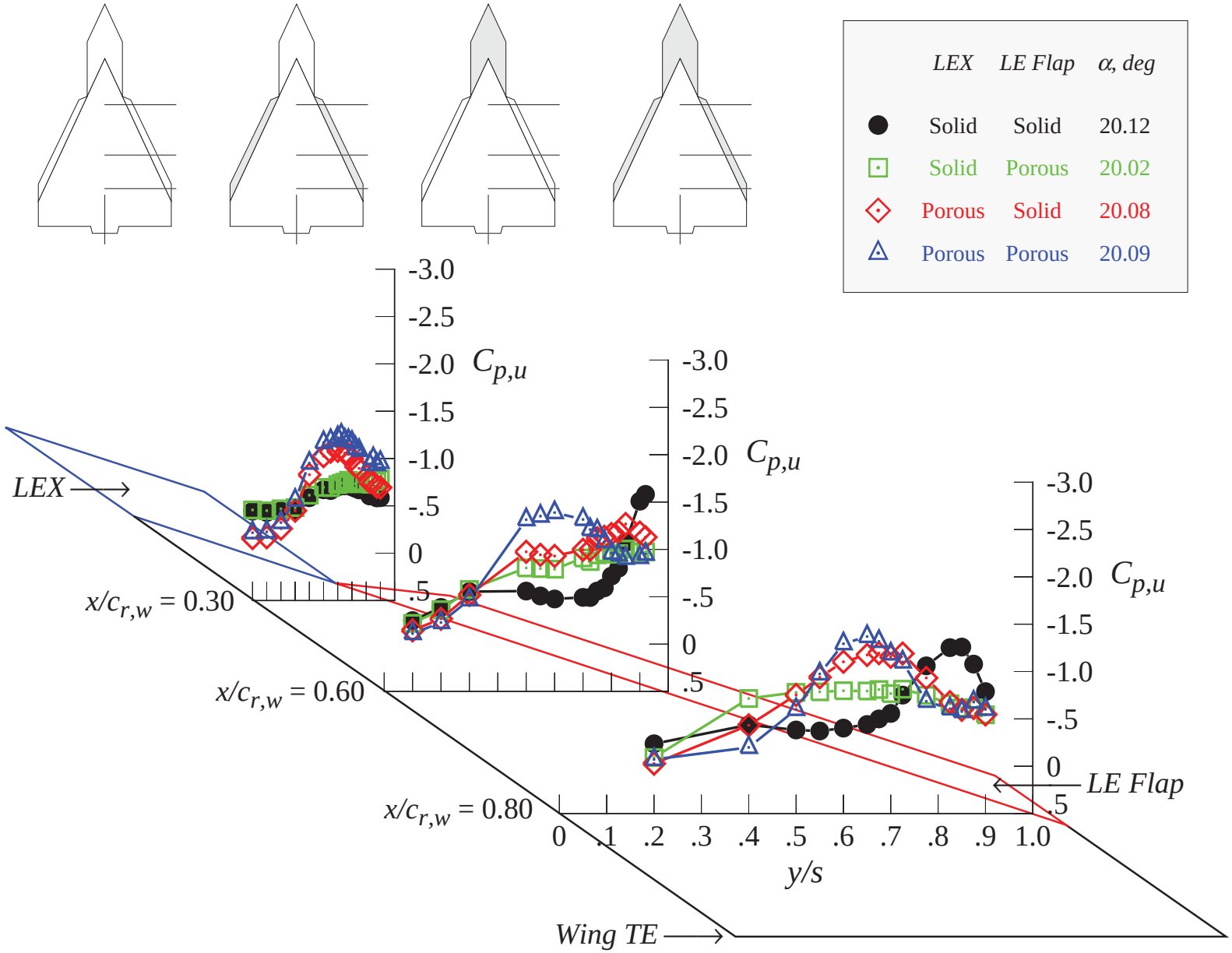

(c) α = 20°

Figure 6. Continued.

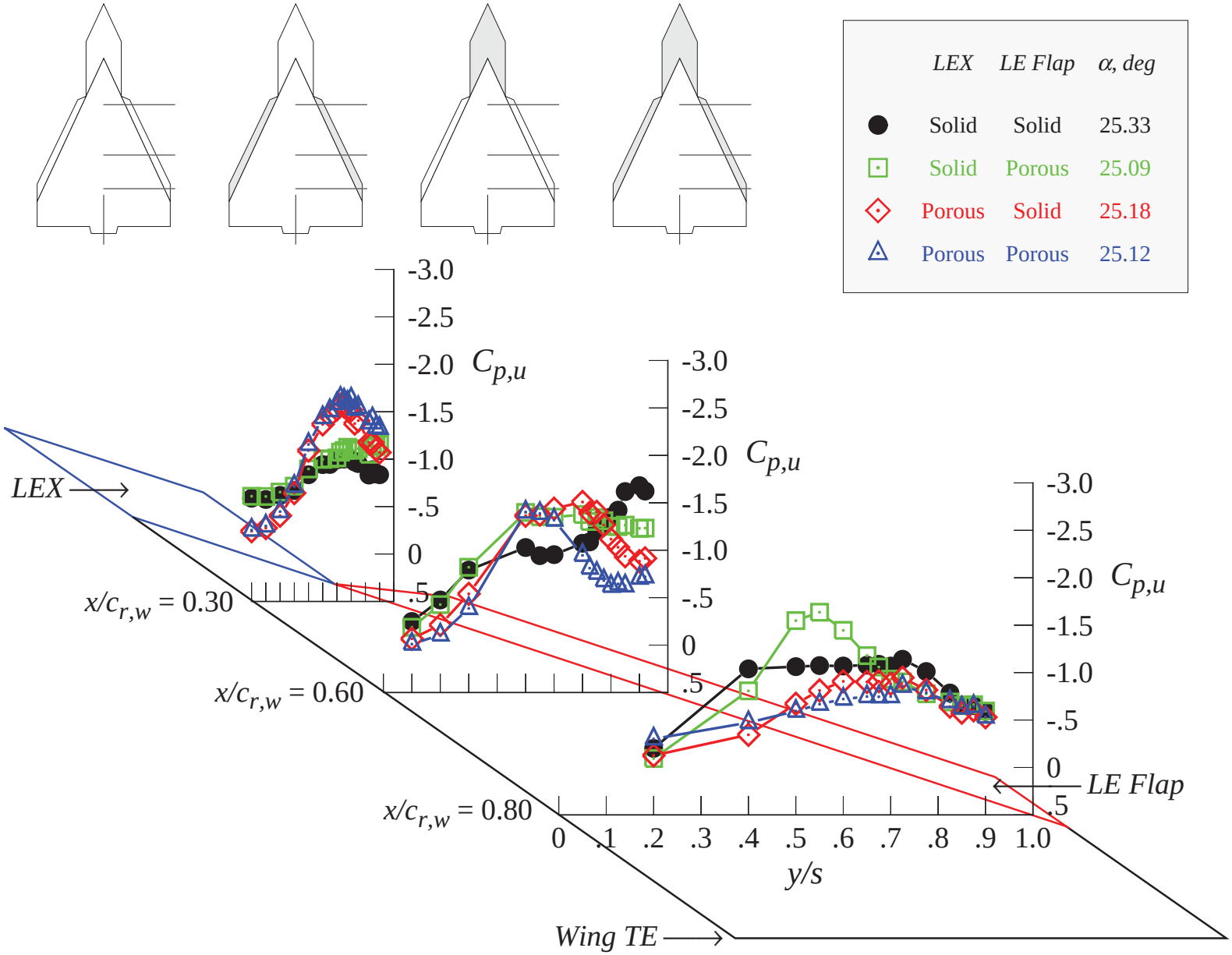

(d) α = 25°

Figure 6. Continued.

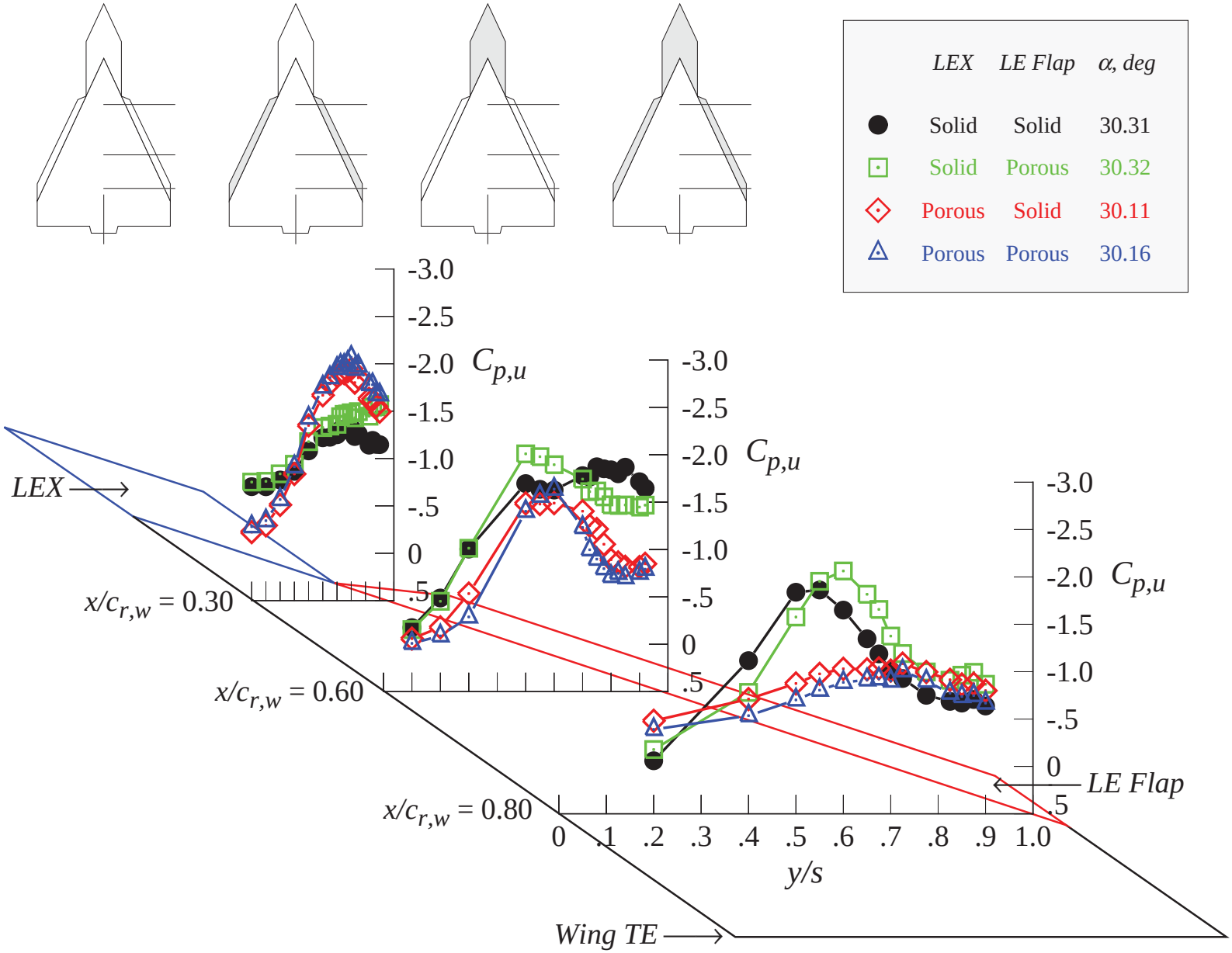

(e) α = 30°

Figure 6. Continued.

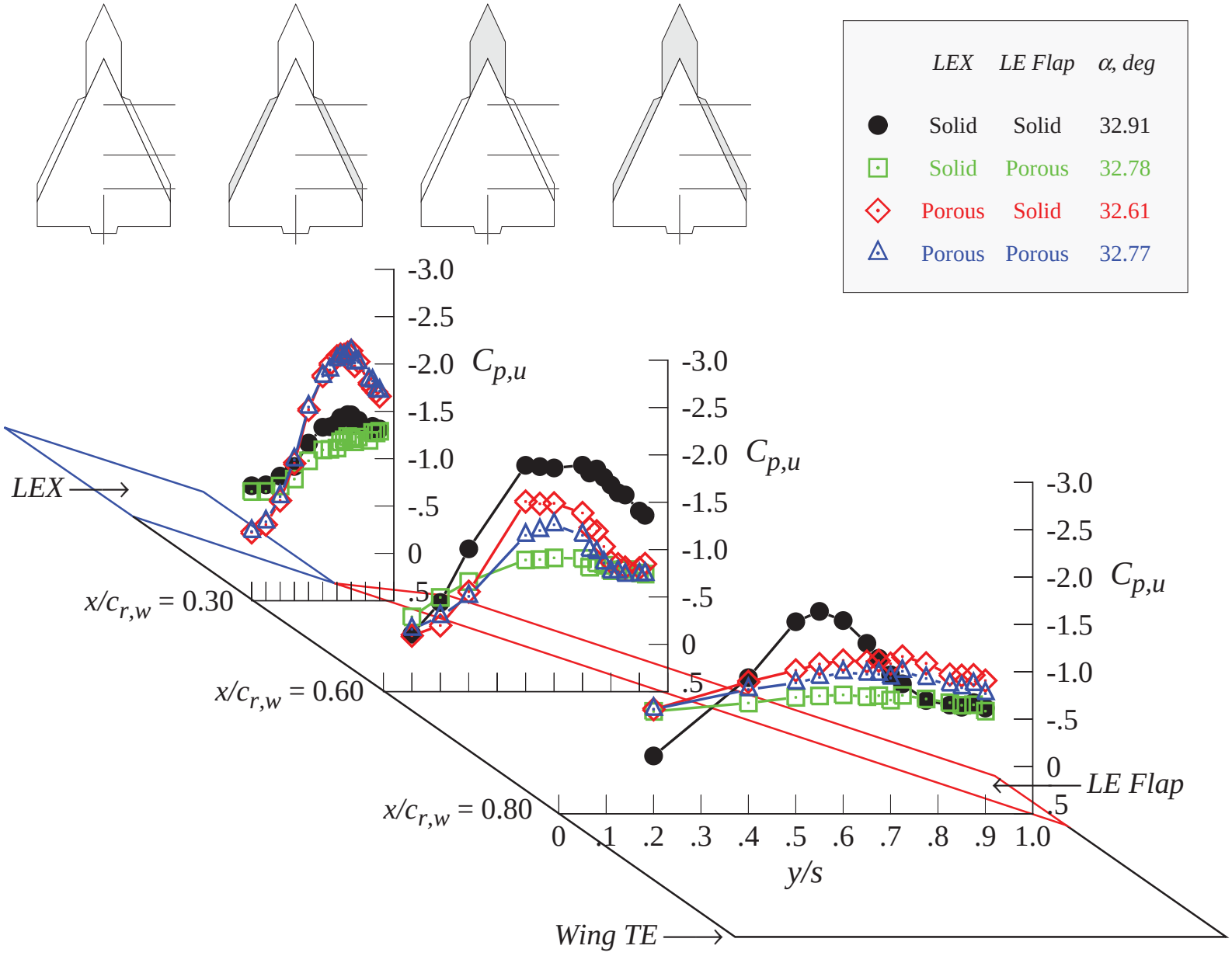

(f) $\alpha = 32.5°$

Figure 6. Continued.

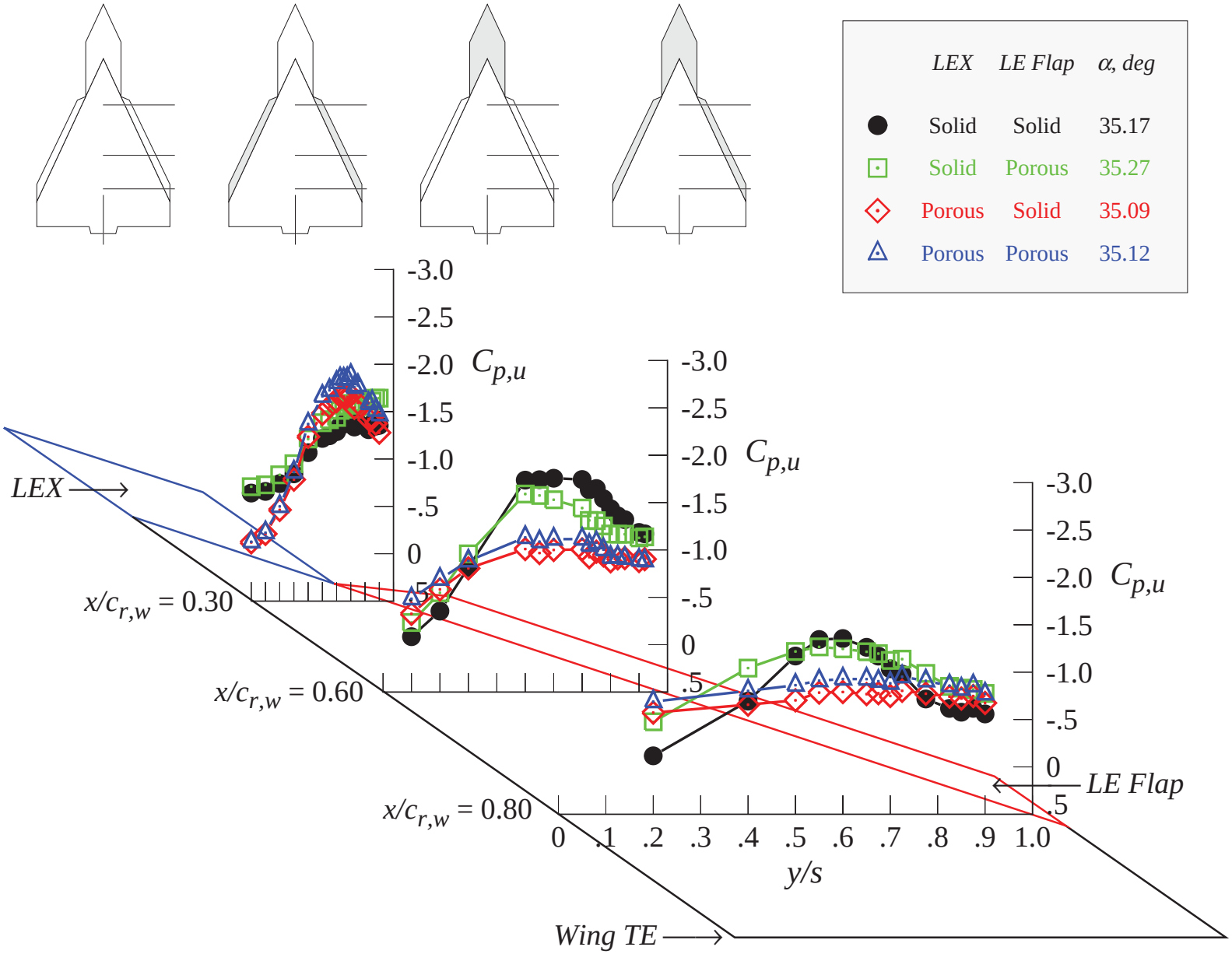

(g) α = 35°

Figure 6. Continued.

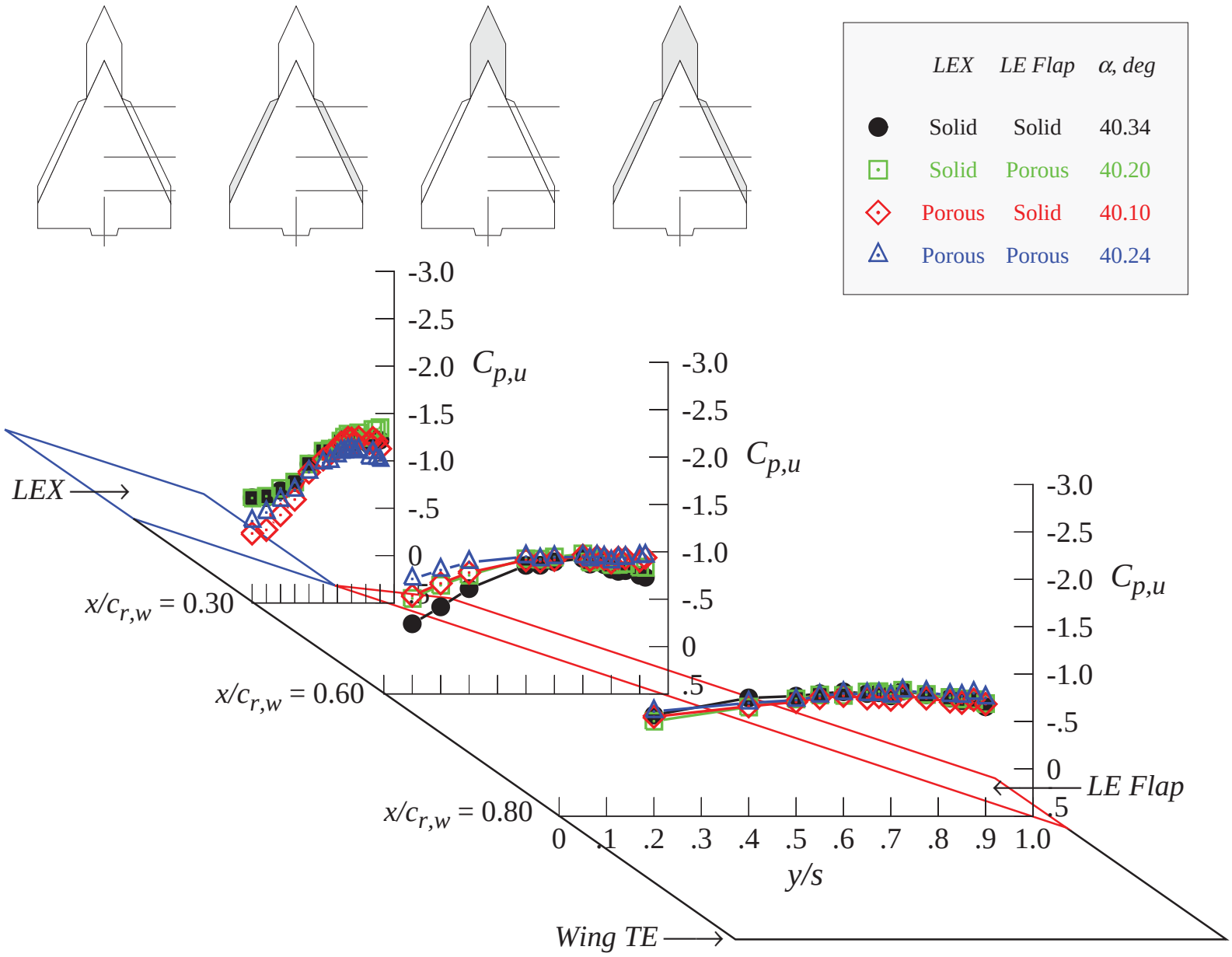

(h) α = 40°

Figure 6. Concluded.

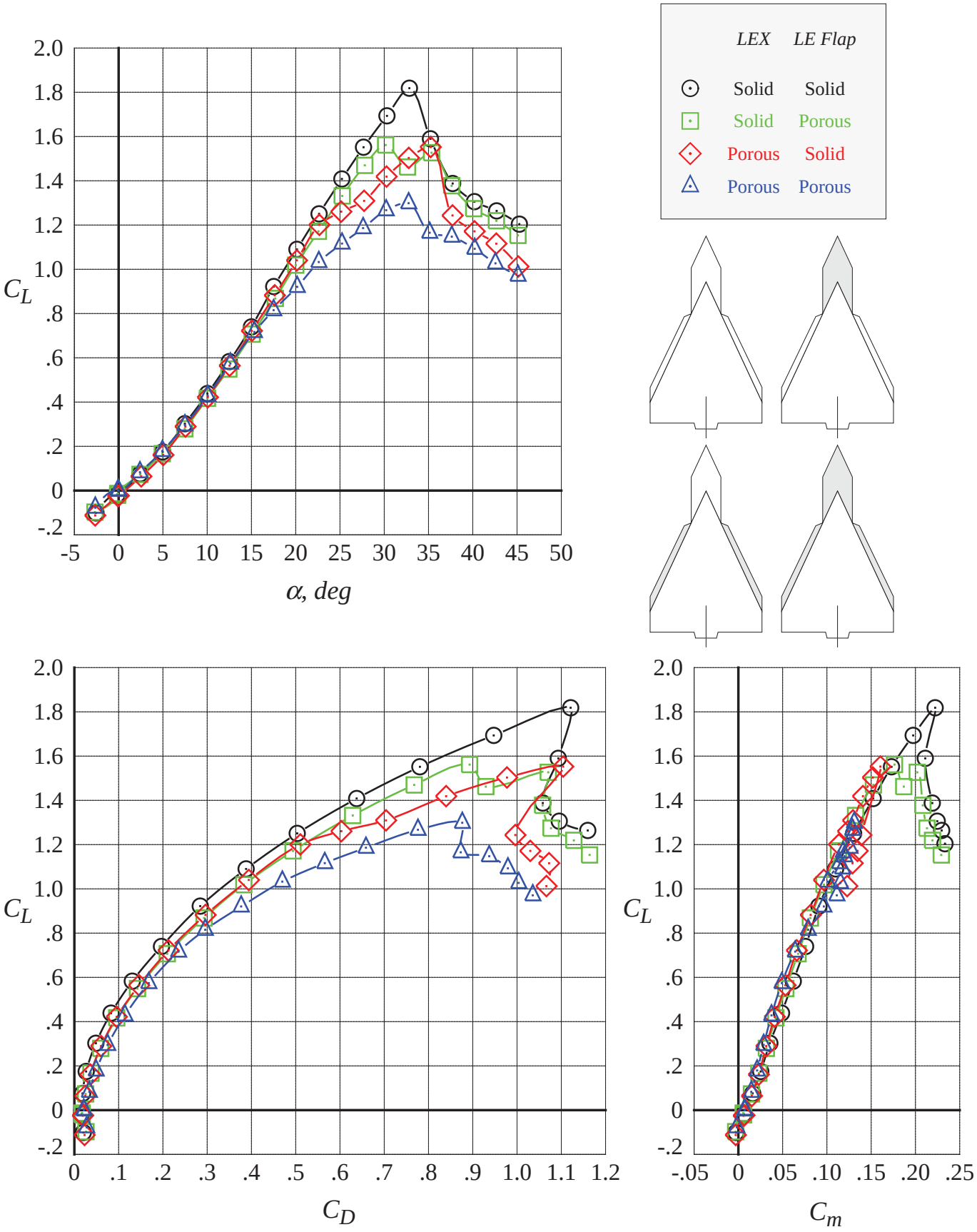

Figure 7. Effect of porosity on the longitudinal aerodynamic coefficients; leading-edge flaps undeflected.

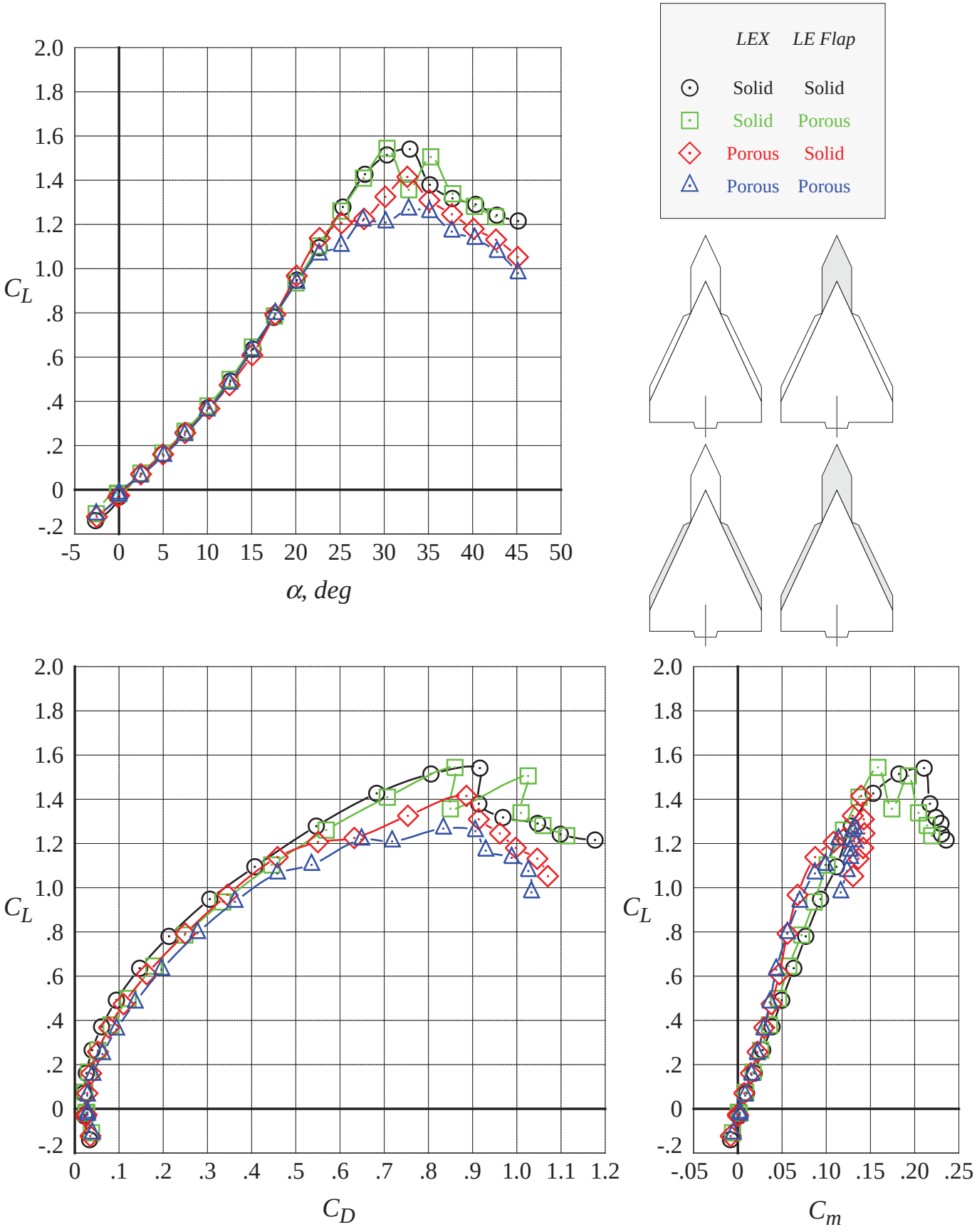

Figure 8. Effect of porosity on the longitudinal aerodynamic coefficients; leading-edge flaps deflected 30°.

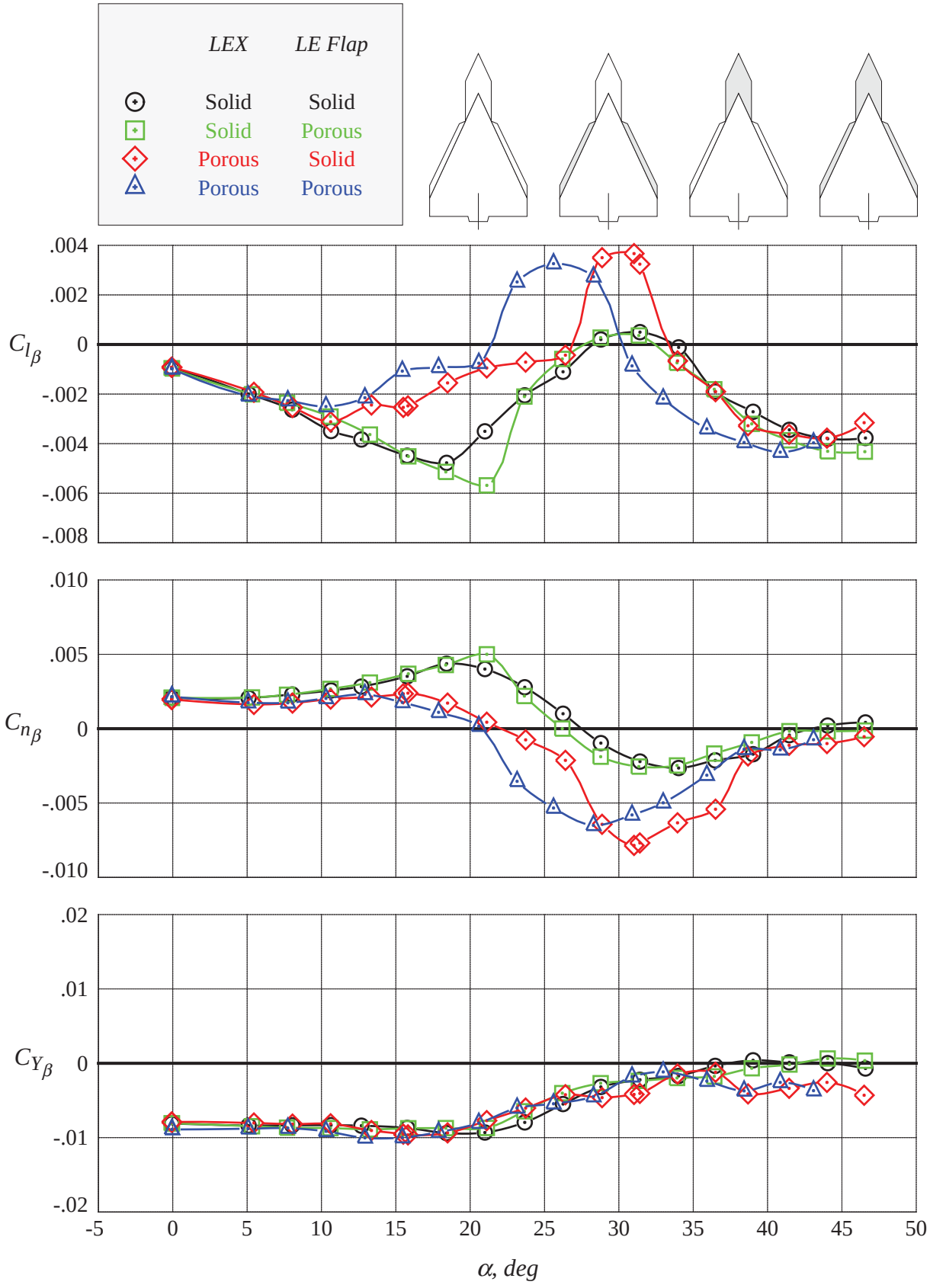

Figure 9. Effect of porosity on the static lateral-directional stability derivatives; leading-edge flaps undeflected.

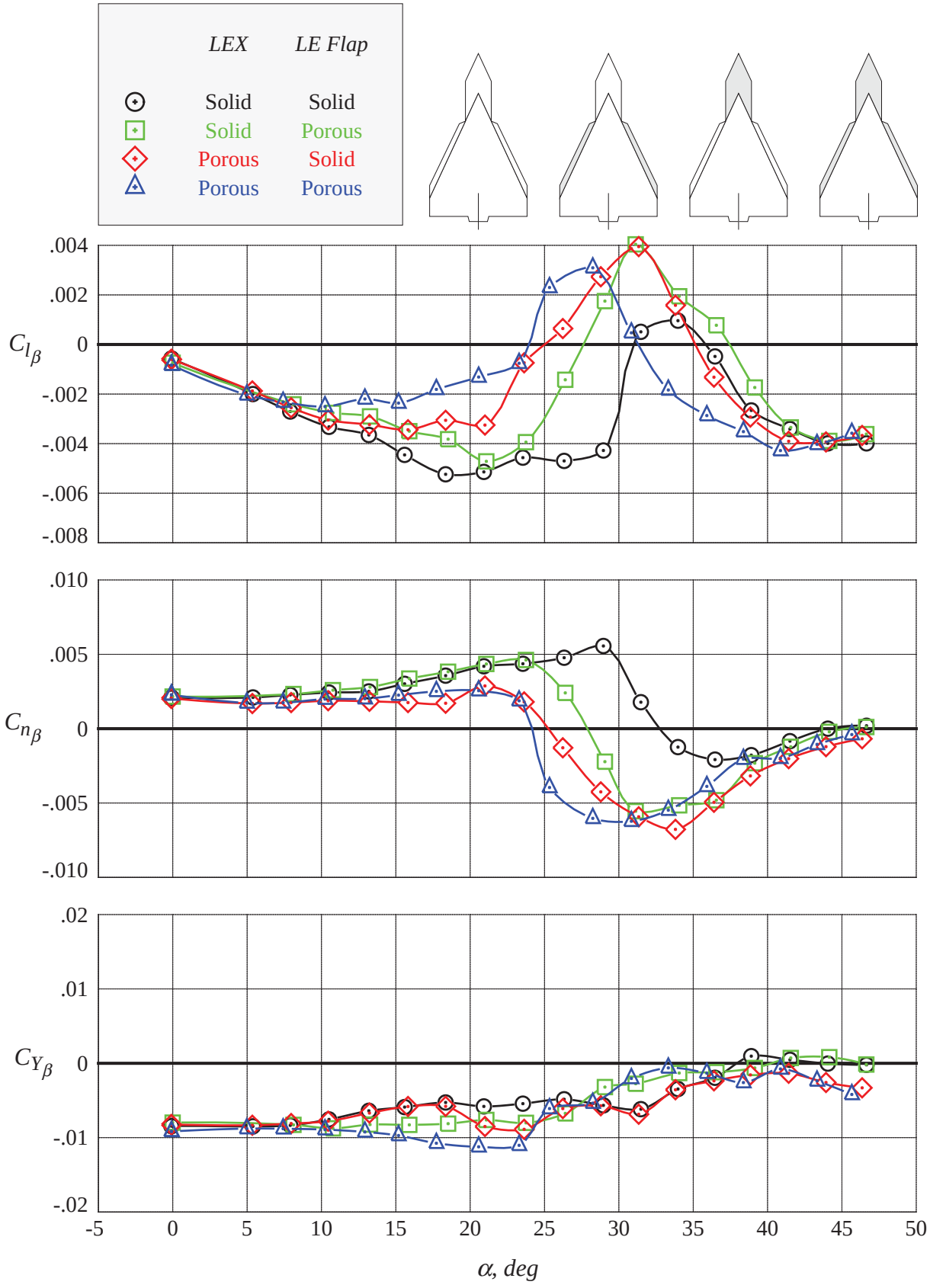

Figure 10. Effect of porosity on the static lateral-directional stability derivatives; leading-edge flaps deflected 30°.

REPORT DOCUMENTATION PAGE

Form Approved
OMB No. 0704-0188

1. REPORT DATE *(DD-MM-YYYY)*
01-03-2017

2. REPORT TYPE
Technical Memorandum

3. DATES COVERED *(From - To)*

4. TITLE AND SUBTITLE
Wind Tunnel Investigation of Passive Porosity Applied to the Leading-Edge Extension and Leading-Edge Flaps on a Slender Wing at Subsonic Speed

5a. CONTRACT NUMBER

5b. GRANT NUMBER

5c. PROGRAM ELEMENT NUMBER

6. AUTHOR(S)

Erickson, Gary E.

5d. PROJECT NUMBER

5e. TASK NUMBER

5f. WORK UNIT NUMBER
147016.03.07.04.02

7. PERFORMING ORGANIZATION NAME(S) AND ADDRESS(ES)

NASA Langley Research Center
Hampton, VA 23681-2199

8. PERFORMING ORGANIZATION REPORT NUMBER
L-20784

9. SPONSORING/MONITORING AGENCY NAME(S) AND ADDRESS(ES)

National Aeronautics and Space Administration
Washington, DC 20546-0001

10. SPONSOR/MONITOR'S ACRONYM(S)
NASA

11. SPONSOR/MONITOR'S REPORT NUMBER(S)
NASA-TM-2017-219596

12. DISTRIBUTION/AVAILABILITY STATEMENT

Unclassified
Subject Category 02
Availability: NASA STI Program (757) 864-9658

13. SUPPLEMENTARY NOTES

14. ABSTRACT

A wind tunnel investigation was conducted in the NASA Langley Research Center 7- by 10-Foot High Speed Tunnel at Mach = 0.20 to determine the effects of passive porosity on the high angle-of-attack aerodynamic and stability characteristics of a generic 65-degree cropped delta wing model. Flow-through porosity was applied to the leading-edge extension (LEX) and wing leading-edge flaps to manipulate the relative strengths and interactions of the LEX and wing vortices.

15. SUBJECT TERMS

Aerodynamics; High angle of attack; Laser vapor screen; Passive porosity; Static stability; Subsonic speeds; Surface pressures; Wind tunnel; Vortex breakdown; Vortex flows

16. SECURITY CLASSIFICATION OF:			17. LIMITATION OF ABSTRACT	18. NUMBER OF PAGES	19a. NAME OF RESPONSIBLE PERSON
a. REPORT	b. ABSTRACT	c. THIS PAGE			STI Help Desk (email: help@sti.nasa.gov)
U	U	U	UU	49	19b. TELEPHONE NUMBER *(Include area code)* (757) 864-9658